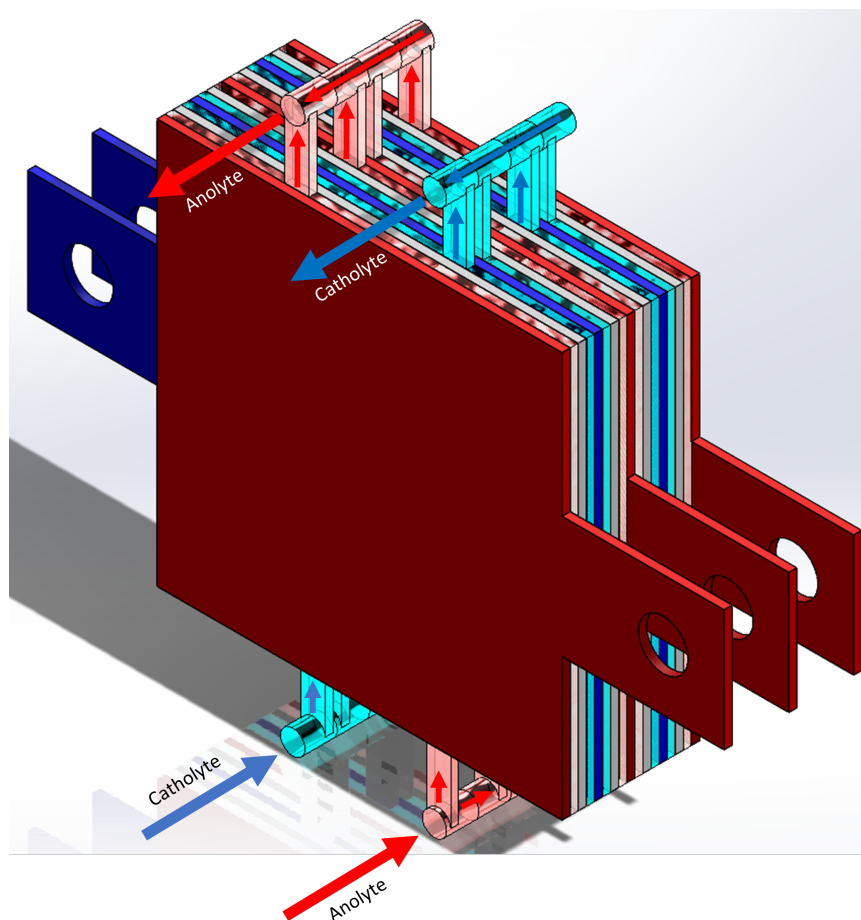


Optimizing the design of a CO₂ electrolyser for producing formate to improve flow distribution and gas bubble flow

Experimental and numerical investigation of several designs

by

Jos van der Maas



Company:	Coval Energy B.V.
Company supervisor:	L.J.P. Legrand
Institution:	Delft University of Technology
Course:	ME55035 ME-EFPT Thesis
Supervisor:	T.J.H. Vlught
Student:	Jos van der Maas
Studentnumber:	4939468
Place and date:	Rotterdam, September 2021

Preface

This report is used to assess the thesis of Energy Fluids and Process Technology (EFPT) students at Delft University of Technology (DUT). This report is written for the assessment committee and Coval Energy B.V. The results of my research and how I arrived at these results are particularly interesting for Coval.

People who are interested in the Computational Fluid Dynamics (CFD) can have a look at chapters 2 and 4. Information about the flow dynamics and gas behaviour inside an experimental setup and the actual reactor can be found in chapters 3 and 5. People who want to know what can be improved in the design can find the conclusions in chapter 6.

I did my internship at Coval, because Coval develops promising technology to turn CO₂ into a valuable product. What also appealed to me is that Coval is a small company, so I was able to learn a lot about the technology.

I want to thank Thijs Vlugt for his support. I am indebted to Coval for this opportunity. I want to give special thanks to Louis Legrand for his guidance. He helped to make this thesis feasible and of better quality. He spend also a lot of energy to take this report to a higher level.

Rotterdam, September 2021
Jos van der Maas

Summary

The world's energy demand is rising as a result of industrial activity and advances in countries around the world. Fossil fuel sources are used to meet this demand for much of the world [1]. The way in which energy is handled causes pollution e.g., CO₂ emissions, inducing climate change, therefore a more sustainable industry is desired [2, 3]. Carbon Capture and Utilization (CCU) is a way to use CO₂ from the atmosphere or which would end up in the atmosphere, limiting its influence on the climate. Sustainable fuels or chemicals can be produced from the captured CO₂, reducing the use of fossil fuels and fossil feedstock [4, 5].

Formic Acid is a favourable product from CO₂ electrolysis. Only 2 electrons are required for one molecule Formic Acid, which results in a high normalized price (\$/electron) [6]. COVAL Energy works on scaling-up and commercialization of CO₂ electrolysis to Formic Acid. Coval has already an operational reactor on lab scale with promising performance, a conversion efficiency up to 90%. Although the reaction kinetics are limited by a poor distribution of reactants on the electrode surface. Previous research by Jos van der Maas showed a highly uneven flow distribution in the cell reactor [7]. Gas bubbles are formed inside the reactor, which likely limit the reaction. Consequences of this poor distribution of reactants and these bubbles are a lower energy efficiency and higher electrical resistance.

The main question of this thesis is: How can the current knowledge of electrolyzers be applied to improve the Coval electrolyser design regarding flow distribution and mitigation of the impact of dissolved gas production? Experiments were performed to gain knowledge about the bubble behaviour in the Coval electrolyser. Computational Fluid Dynamics (CFD) was used to screen design ideas on liquid distribution. Promising designs were assessed in a flow and gas bubble visualisation experimental setup, in which also the bubble behaviour was investigated. Finally, prototypes to be tested in the high pressure reactor were produced.

Two auspicious designs were found. The first design has channels in the inter electrode gap. The results showed that with channels the velocity variation over the cell width was reduced. The second design has a manifold like geometry in a calm zone before and after the interelectrode gap. This resulted in an almost constant velocity over the cell width for the entire cell. Additionally, a larger inlet and outlet pipe to and from the cell improves flow homogeneity and reduces pressure drop in these pipes. The gas fraction in the cell can be kept low by sloping the top part of the cell towards the outlet.

A next step is to assess both designs in the high pressure reactor. Particular attention should be paid to the manufacturing of the design to avoid leakage and mechanical deterioration. It is recommended to measure pressure drop over the cell for better assessment of the designs.

Contents

Preface	ii
Summary	iii
Nomenclature	v
List of Figures	vi
List of Tables	ix
1 Introduction	1
1.1 CO ₂ electrolyser principle	1
1.2 Flow distribution	4
1.2.1 Design guidelines	4
1.3 Bubble origination and behaviour	5
1.3.1 The (un)favourable effects of bubbles	5
1.3.2 Theoretical bubble behaviour	6
1.3.3 Formation and development	8
1.3.4 Behaviour in the bulk	8
1.3.5 Mitigation	10
1.3.6 Design guidelines	11
1.4 Approach of this study	11
2 Numerical methodology	13
2.1 Assumptions	13
2.2 Governing equations	13
2.3 Geometry and mesh	14
3 Experimental methodology	17
3.1 Bubble visualization in the high pressure reactor	17
3.2 Flow visualization cell	20
4 Screening of designs with CFD modelling	23
4.1 List of screened adjustments	23
4.2 First CFD screening	24
4.3 Second CFD screening	28
4.4 Conclusion and final selection of designs	32
5 Experimental results and discussion	33
5.1 Flow distribution	33
5.2 Bubble behaviour	38
5.3 Bubble visualization in the high pressure reactor	41
5.4 Prototyping	43
6 Conclusions and recommendations	47
Bibliography	51
A 2D drawings	55

Nomenclature

Symbol	Definition	Unit
a	acceleration	m s^{-2}
b	x coordinate of the inlet	m
c	y coordinate of the inlet	m
Bo	Bond number	
Ca	Capillary number	
f	body force	N m^{-3}
F	force vector	N
Fr	Froude number	
g	gravitational acceleration	m s^{-2}
h	thickness	m
I	intensity	W m^{-2}
L	length	m
\hat{n}	normal vector	
p	pressure	N m^{-2}
r	radius	m
Re	Reynolds number	
t	time	s
T	stress tensor	N m^{-2}
\mathbf{u}	velocity vector	m s^{-1}
u	velocity in x direction	m s^{-1}
\dot{V}	flow rate	$\text{m}^3 \text{s}^{-1}$
v	velocity in y direction	m s^{-1}
w	velocity in z direction	m s^{-1}
w	width of the cell	m
We	Weber number	
μ	dynamic or shear viscosity	$\text{kg m}^{-1} \text{s}^{-1}$
ρ	density	kg m^{-3}
σ	surface tension	N m^{-1}
σ	standard deviation	
ω	angular velocity	rad s^{-1}
∇	vector differential operator	

Subscript	Definition
am	added mass
B	bubble
b	buoyancy
d	drag
e	entrance
g	gravity
G	gas phase
L	liquid phase
l	lift

List of Figures

- 1.1 2D drawing of the present flow channel between the electrode and membrane with an in plane thickness of 2 mm. The green-outlined square is the electrode. The electrolyte enters perpendicular to the sheet through the 6 mm hole at the bottom. The electrolyte then flows upwards along the electrode. The electrolyte leaves perpendicular to the sheet through the 6 mm hole at the top. Figure 1.4 shows the location of this flow channel in the electrolyser stack. 4
- 1.2 A rising, accelerating gas bubble in the flowing electrolyte near a vertical electrode wall with the forces acting on it. With bubble acceleration \mathbf{a}_b , bubble velocity \mathbf{v}_b , liquid velocity \mathbf{v}_L , gravitational acceleration g , angular velocity $\boldsymbol{\omega}$, the pressure inside the bubble p_G , the pressure in the liquid p_L , the density of the gas ρ_G and the density of the liquid ρ_L . The forces acting on the bubble: the buoyancy force \mathbf{F}_b , the lift force \mathbf{F}_l , the added mass force \mathbf{F}_{am} , the gravity \mathbf{F}_g and the drag force \mathbf{F}_d 6
- 1.3 Processes of the formation and movement of bubbles. (a) Supersaturation is the prerequisite for bubble nucleation. If there is locally supersaturation, the dissolved gas can either transfer to the bulk or nucleate on the cell surface. This scheme shows the possible routes for dissolved gas. (b) When a bubble detaches from the cell surface, it will rise in the electrolyte. The bubble velocity with respect to the electrolyte depends on its diameter. A detached bubble can still grow by absorbing dissolved gas or by coalescing with other bubbles. 9
- 1.4 Simplified representation of the present electrolyser stack, the electrolyte flows from bottom to top. The solid red and solid blue plates are the anode and cathode respectively, the solid grey sheets are the membranes. The dimensions of the active area are 0.01 m^2 . (a) Side view, the height of the assembly is 0.141 m , (b) top view, (c) detail of the layers in 1.4a, and (d) isometric view of the stack with the streams indicated. 12
- 2.1 The flow domain between the electrode and the membrane. The electrolyte enters the interelectrode gap perpendicular to the sheet through the hole at the bottom. Next, the electrolyte flow upwards through the gap. Finally, the electrolyte leaves the gap through the hole at the top perpendicular to the sheet. A plug flow is desired in this domain, so a flow front like a horizontal plane moving purely upwards. One could imagine the fluid going from the green, to the blue and the red line successively and having no velocity in horizontal direction. In that case each fluid 'package' has the same residence time in the inter electrode area. The interelectrode gap is 0.1 m wide. 14
- 2.2 Detail of the top part of the conventional cell with the outlet pipe and its connection to the square cell. The cell has a thickness of 2 mm and the outlet pipe a diameter of 6 mm. (a) Chopped geometry to guide the mesher. (b) The circumference of the pipe is adjusted to avoid a cusp. 15
- 3.1 The setup to visualize bubbles and to capture the high pressure reactor outflow. The see-through diameter is 32 mm 18

3.2	Flow visualization setup which allows to study both flow distribution and gas bubble behaviour. The see-through area of the visualisation cell is 0.01 m^2 . Flow distribution is studied using deionized water and an indigo carmine solution. Bubble behaviour can be studied using the indigo carmine solution and the air pump.	21
4.1	Several designs screened with CFD. The red and the blue circles at the bottom and top represent the inlet and outlet respectively, both perpendicular to the cell. All these cells have a width of 100 mm and an inlet and outlet pipe diameter of 6 mm . (a) The present design. (b) The design with a calm zone at the entrance and exit of the cell. The calm zone can be divided in three parts in the flow direction (bottom to top): (i) proportional division of the entering fluid, (ii) distribution of the fluid to the full cell width, and (iii) the actual calm zone of the same width as the cell. (c) A design with channels to guide flow. (d) A side view of a design with constrictions at the beginning and end of the cell to promote equal flow distribution over the cell width.	24
4.2	The velocity at various locations in the cell for the calm zone design with 2 mm cell thickness. (a) The locations of the velocity measurements: green ($y = -0.044 \text{ m}$), blue ($y = 0 \text{ m}$) and red ($y = 0.044 \text{ m}$). (b) The velocity in contours in the cell at $z = 0 \text{ m}$ (the middle plane). (c) The vertical velocity over the cell width (0.1 m) at the three locations.	25
4.3	The vertical velocity at $y = -0.044 \text{ m}$ to compare modelled design ideas. (a) The effect of several numbers of channels, compared to the starting point design (green line). (b) The effect of the cross sectional area of the inlet and outlet pipe to and from the cell. (c) The effect of varying the cell thickness. The increase in velocity across the width of the cell is approximately proportional to the decrease in cell thickness. The actual increase in velocity is higher. (d) The effect of changing the aspect ratio.	26
4.4	Effect of several parameters on the homogeneity and pressure drop investigated in the first modelling iteration: (a) The effect of cell thickness, (b) the effect of the number of channels, (c) the effect of the cross sectional area of the inlet and outlet pipe, and (d) the effect of the aspect ratio.	27
4.5	Variations to the calm zone design. (a) The calm zone design as studied in the first modelling iteration. (b) A smaller angle (60°) in the first part of the calm zone (1). (c) Modification in the top part of the calm zone (2).	29
4.6	A variation to the design with the channels, the channel length is varied over the cell width.	29
4.7	The vertical velocity at $y = -0.044 \text{ m}$ to compare the combination of design ideas. (a) Different calm zones and a larger cross sectional area of the inlet and outlet pipe combined. (b) The calm zone with larger inlet and outlet pipe versus a design which has a constriction too. (c) Designs with channels, larger inlet and outlet pipe and a constriction, compared to the design with channels in the first modelling round. (d) Aspect ratios of 0.5 , 1 and 2 compared.	30
4.8	Effect of several parameters on the homogeneity and pressure drop investigated in the second modelling iteration: (a) the effect of the number of channels, and (b) the effect of the aspect ratio.	32
5.1	Contours of the ink arrival time measured from the cell inlet at the bottom. (a) Conventional design, as shown in figure 4.1a. It takes $\sim 7 \text{ s}$ for the ink to reach the outlet and it takes much longer than 15 s to reach the whole cell. The white indicates the area that is not reached within 15 s . Homogeneity: 0.3 . (b) Conventional design with net, almost the full cell is reached within 10 s . Homogeneity: 0.4	34

5.2	The effect of channels, contours of ink arrival time for the calm zone design and a design with channels. (a) Calm zone with 2 mm cell thickness, homogeneity: 0.7. (b) Design with a calm zone and 15 channels, homogeneity: 0.6.	34
5.3	The effect of cell thickness with a net, contours of ink arrival time for the calm zone design with a net. (a) 0.5 mm cell thickness. The white dots indicate that the net is touching the cell walls. Homogeneity: 0.8. (b) 2 mm cell thickness. The fluid follows preferential channels. Homogeneity: 0.9.	34
5.4	A manifold like geometry in the calm zone to distribute the flow equally over the cell width. (a) The dark grey indicates the electrode and the electrolyte flows upwards in the channel created by the light grey spacer. The outer diameter is 0.19 m. (b) The red circle indicates where the electrolyte enters the 1 mm interelectrode gap. A baffle is placed right above this inlet. The manifold consists of two beams with oval holes.	35
5.5	The effect of an advanced calm zone, contours of ink arrival time. (a) For a design with a constriction in the calm zone, homogeneity: 0.8. (b) For a design with a manifold like geometry in the calm zone, homogeneity: 1.4.	35
5.6	Ink arrival time at $y = -0.044$ m. (a) The green line is the location where the ink arrival time is measured. (b) The ink arrival time over the cell width plotted for the two present configurations. The blue graph does not cover the full width of the cell, because the recording was stopped before the ink arrived over the full cell width.	36
5.7	Ink arrival time at $y = -0.044$ m for all the experimentally assessed design ideas. This is the extended version of figure 5.6b. (a) Shows an overview of all tested designs. (b) Focusses on the effect of calm zone, interelectrode gap and larger pipes. (c) Presents the effect of a geometry in the calm zone or interelectrode gap.	37
5.8	Graphical representation of the homogeneity values for all the experimentally assessed design ideas. The homogeneity is defined in the same way as in equation (4.1), but now all y values are taken into account.	37
5.9	The repeating cycle of bubbles in the experimental visualisation cell without a net. (a) Bubbles entering the cell from the inlet at the bottom and rising to the top, $t = 9$ s. (b) Gas accumulation at the top of the cell till the accumulated bubble reaches a critical size, $t = 13$ s. (c) The accumulated bubble is escaped from the cell and this cycle repeats itself, $t = 16$ s.	39
5.10	The experimental bubble behaviour with a net, the bubbles are routed by the net. (a) $t = 0$ s, (b) $t = 50$ s and (c) $t = 60$ s, the gas fraction shows only minor variations.	39
5.11	Gas fraction in the cell for the experimentally assessed design ideas over a period of 60 s (a). Detail view of: (b) the designs without and with a calm zone with 2 mm thickness, and (c) the designs with channels and a geometry in the calm zone.	40
5.12	Different types of bubbles seen through a 32 mm diameter sight glass in the reactor outflow line of the high pressure electrolyser setup. For the experimental setup and the location of the sight glass see figures 3.1 and 5.13. (a) A big bubble, (b) small bubbles, and (c) smoke.	42
5.13	Part of the higher pressure electrolyser setup showing the anolyte and catholyte discharge lines from the reactor to the sight glass. The outer diameter of the lines is 6.35 mm.	43

5.14	A front view of the design with channels which is an assembly of a tin plate (dark grey) and two 3D printed PLA inserts. The electrolyte enters perpendicular to the cell in the bottom light coloured part where it is spread across the 15 channels. Then the electrolyte flows vertically to the top through the channels. In the top light coloured part all the electrolyte is gathered and leaves perpendicular to the cell. The 12 holes are used to mount the electrode in the stack. The outer diameter is 190 mm, the total width of the electrolyte flow channel is 100 mm and the a single channel has a width of 6.2 mm.	44
5.15	The stack with the channel design mounted. The outer diameter of the parts is 190 mm and the thickness of the cathode and anode is 5 mm. The membrane which separates the anolyte and the catholyte is located between the anolyte spacer and the cathode.	44
5.16	The result of chemical and mechanical loading on the insert and spacer. (a) Lamination of the insert, probably as a result of the acidic or alkaline environment. The channel width of this design is 6.2 mm. (b) Deformation of the insert because the fit in the cavity was too tight. (c) A crack in the spacer as a result of mechanical loading.	45
6.1	Graphical representation of the experimental homogeneity and gas removal values for the experimentally assessed design ideas. The homogeneity is defined in the same way as in equation (4.1), but now all y values are taken into account. . . .	48

List of Tables

2.1	Overview of key parameters of the CFD simulations	14
3.1	Settings for the experiments with the high pressure electrolyser. Experiment 1 to 6 were ran with CO ₂	19
4.1	Overview of the characteristics of the design ideas considered in the first modelling round.	27
4.2	The characteristics of the designs considered in the second modelling iteration.	32
5.1	Overview of the findings when performing the experiments in table 3.1. A hypothesis is given for each observation.	42

1. Introduction

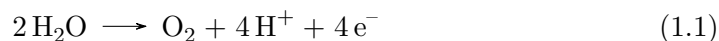
The world's energy demand is rising as a result of industrial activity and advances in countries around the world. Fossil fuel sources are used to meet this demand for much of the world [1]. The current handling of energy causes pollution, including CO₂ emissions. These emissions induce climate change, so a more sustainable industry is desired [2, 3]. Carbon Capture and Utilization (CCU) is a way to use CO₂ from the atmosphere or which would end up in the atmosphere, limiting its influence on the climate. Sustainable fuels or chemicals can be produced from this captured CO₂, reducing the use of fossil fuels and fossil feedstock [4, 5].

CO₂ electrolysis received a lot of attention in recent years due to several benefits: (i) renewable energy can be used to drive the process, (ii) the electrolysis conditions are easily controlled, and (iii) the electrolysis system is compact and is scalable [8]. Electrolysis is a separation technique which uses an electrical potential to drive a chemical reaction. Products of CO₂ electrolysis are substances consisting of C, H and/or O. The electrode material, which acts as a catalyst, influences what substances are produced.

1.1. CO₂ electrolyser principle

There are two main techniques for CO₂ electrolysis, aqueous and gaseous electrolysis. In aqueous electrolysis, CO₂ is dissolved in the electrolyte before entering the reaction cell. The electrolyte is the liquid fed to an electrochemical reactor containing the reactants, after reaction it contains also electrolysis products. Gaseous CO₂ can be electrochemically converted using a porous, so-called gas diffusion, electrode. The full liquid reactant electrolysis is a more mature and better understood method than the gaseous electrolysis. It is not fully known how electrolysis of gaseous CO₂ takes place and therefore not entirely clear how this cell should be optimized [9]. Formic Acid (HCOOH) is a favourable product from CO₂ electrolysis. Only 2 electrons are required for HCOOH production which results in a high normalized price (\$/electron) among other major CO₂ electrolysis products [6]. HCOOH can be widely used [10] and it has also a high conversion efficiency [11]. KOH is a non-toxic, inexpensive electrolyte which can be used for CO₂ electrolysis to HCOOH. One of the catalyst materials for conversion to HCOOH is Sn, it is attractive because promising results were obtained [10] and it is earth-abundant [12].

When CO₂ reacts to formic acid (HCOOH) or formate (HCOO⁻) in a KOH electrolyte using a bipolar membrane, the reactions are:



Water is split at the anode (reaction 1.1) and the bipolar membrane (reaction 1.2). The products at the anode are oxygen, hydrogen ions and electrons. The membrane transports its produced H⁺ to the cathode and its produced OH⁻ to the anode side. The CO₂ reduction reaction takes place at the cathode side (reaction 1.3). In the electrolyte is an equilibrium reaction which is influenced by the pH, this reaction converts HCOOH into HCOO⁻ (equation 1.5).

CO₂ electrolysis has several benefits, but there are challenges to overcome before it can be industrialized, these challenges are:

- Keeping the pH stable [9]. The pH influences which product is produced, so to obtain a

desired product the pH should remain in a certain range.

- Developing membranes with low ohmic resistance and product leakage, and that do not limit mass transfer [4, 9]. The lower the ohmic resistance, the lower the required potential to drive the reaction and thus the electricity cost. If product leaks, unwanted reactions can occur and it may become harder to capture the product from the reactor outflow. The membrane limits mass transfer if reaction (1.2) is the limiting factor in the full reaction. The key for a successful membrane is that it has a low resistance for the transfer of desired species and a high resistance to transfer any other specie.
- Reducing the cell resistance, both the ohmic resistance between the electrodes and the resistance for ion supply to the electrodes [13]. The importance is already explained in the previous challenge. H^+ are required for the CO_2 reduction reaction at the cathode. If the resistance for ions supply is high this reaction is slowed down.
- A high reaction rate at low overpotential [13]. The overpotential is the difference between the thermodynamic reduction potential and the experimentally observed potential i.e., the difference between the theoretically required potential to drive the reaction and the actual potential required. This challenge is linked to a low ohmic resistance of the cell. As stated before a low potential results in low electricity costs. The potential depends also on the catalyst material(s), membrane and distance between the electrodes.
- Reducing capital cost by Increasing the current density which reduces the required area and thereby capital cost [13].
- Obtain economically viable products by increasing the overall energy efficiency [13].
- Avoiding the competing formation of undesired product (e.g. H_2) [14]. Unwanted product consumes electrical energy lowering the efficiency.
- Improving the electrode stability and lifetime [4]. The electrode surface which acts as a catalyst can corrode and erode, reducing the performance and increasing operational cost.
- Developing electrodes which require low overpotentials [4]. The lower the overpotential, the lower the electricity cost.
- Producing valuable products at both the anode and cathode [4]. The production of by-products is almost insurmountable. Valuable by-products can make the process more economically attractive.
- Obtaining products in high concentrations to minimize downstream separation costs [4].
- Avoiding mass transfer limitations at the electrode surface due to poor flow distribution [4].
- Producing chemicals with 2 or more C atoms, which have a higher commercial value than chemicals with a single C atom [15].

A lot of attention has been paid to the catalytic material to meet these challenges. New catalyst materials are explored, and performance dependence on morphologies and surface properties are studied [10]. It was shown that mesoporous Sn/SnO_x is superior to the electroplated Sn or Sn foil as electrode catalyst for HCOO⁻ production. The catalytic performance is related with the microstructure of the catalyst. An efficiency of 90% was reached for HCOO⁻ formation with the mesoporous Sn/SnO_x catalyst. This performance is attributed to the high specific area and the surface SnO_x layer of the catalyst. Research is also being done to high pressure electrolysis and the tuning of the electrolyte concentration.

Membranes are studied too, three types are currently applied: anion exchange membranes (AEM), cation exchange membranes (CEM) and bipolar membranes (BPM). The latter reduces the requirements for catalyst, as a result of which the electrode cost can be reduced [16].

The startups working in the field of electrochemical reduction of CO₂ prove that it is an important topic. The startups focus on the commercialization of CO₂ electrolysis. Here follows a list of startups and companies with their key features:

- CERT Systems Inc is a startup working on the production of several chemicals from CO₂. Gaseous CO₂ is converted into CO using Ag as a catalyst in alkaline, high pressure electrolysis. Other products are C₂H₄ with a Cu catalyst and HCOO⁻ with a SnS_x or Pd catalyst. Abundant nonmetal catalysts which can replace scarce resources are explored. Work is also being done on optimizing the oxygen evolution reaction at the anode [17].
- Dioxide materials is a startup working on CO₂ reduction to HCOOH. This startup has developed an ionomer and anion exchange membrane. An ionomer is a plastic that because of its ionic bonding action is capable of conducting electric current. Lab scale electrolysers, membranes, gas diffusion layers and ionomers are offered for sale [18].
- Opus 12 is a startup which focusses on several electrolysis products. CO is produced using a gas diffusion layer and an Ag catalyst, C₂H₄ is produced using a graphene/nitrogen or Cu catalyst, and H₂ using Pt catalyst [19].
- Siemens Energy works on electrolysis of CO₂ to CO. Together with Evonik Siemens Energy has built and operates a pilot plant [20].

Purification is required as the electrolyser does not produce pure HCOOH or HCOO⁻. Whether formic acid or formate is produced depends on pH inside the electrochemical reactor, for pH<3.75 formic acid leaves the reactor as dissolved salt. The salt will almost completely dissociate into the formate form if the CO₂ reduction is performed at alkaline conditions (i.e. pH>3.75). The first step in purification is flashing to ambient pressure whereby remaining CO₂ leaves the solution. Liquid-liquid extraction can be used to separate the formic acid from the other substances. Electrodialysis can be used to produce formic acid from formate. The formate is present in the reactor outflow as potassium formate if KOH electrolyte is used. Potassium formate is a salt that has already an application as deicer. The formic acid route, so pH>3.75, is economically more attractive because of limited downstream processing cost [4].

COVAL Energy works on scaling-up and commercialization of CO₂ electrolysis to HCOO⁻. Coval applies high pressure electrolysis, with CO₂ dissolved in KOH electrolyte using a BPM and Sn electrodes. Coval has already an operational reactor on lab scale with promising performance, a conversion efficiency up to 90%. Figure 1.1 shows a 2D drawing of the present flow channel between the electrode and membrane.

Although the reactor shows promising performance, the reaction kinetics are limited by a poor distribution of reactants on the electrode surface. Previous research by Jos van der Maas showed a highly uneven flow distribution in the cell reactor, especially for higher flow rates [7]. In addition, gas bubbles are formed, which likely limit the reaction when bubbles get stuck in the reactor. Bubble formation is possibly a result of a local lack of CO₂ due to maldistribution of reactants. Lack of CO₂ shifts the reaction selectivity towards H₂ evolution and dissolved H₂ easily nucleates on the electrode surface. Consequences of this poor distribution of reactants and these bubbles are a lower efficiency and higher ohmic resistance.

Further research is required to prepare Coval's technology for pilot scale testing because of the limitations of the present design. The goal of this study is to optimize the cell reactor design by improving flow distribution and mitigating the impact of dissolved gas production. This study contributes primarily to the challenge of avoiding mass transfer limitations due to poor flow distribution. It focusses also on the challenges of reducing the resistance for electrical current and ion supply, and avoiding competing formation of unwanted product. Before proceeding to the drawing table, the state of the art of electrolysis is reviewed concerning flow distribution and gas bubbles. Section 1.4 discusses and motivates the approach of this study.

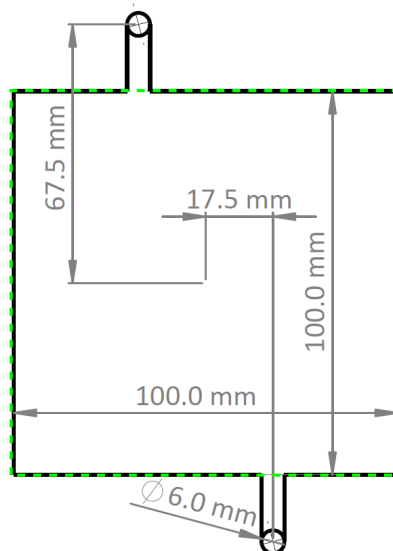


Figure 1.1: 2D drawing of the present flow channel between the electrode and membrane with an in plane thickness of 2 mm. The green-outlined square is the electrode. The electrolyte enters perpendicular to the sheet through the 6 mm hole at the bottom. The electrolyte then flows upwards along the electrode. The electrolyte leaves perpendicular to the sheet through the 6 mm hole at the top. Figure 1.4 shows the location of this flow channel in the electrolyser stack.

1.2. Flow distribution

Uniform supply of species to react and removal of reaction products everywhere in the reactor, is essential for electrolysis reactor performance. So a homogeneous flow with a narrow residence time distribution is preferred. The mass transport regime close to the electrode surface is crucial in the process. This mass transport is improved by (i) a high relative velocity between electrode and electrolyte and (ii) a high electrode area [21].

1.2.1. Design guidelines

Various electrolyser design guidelines can be derived from the studies carried out. Geometric factors are considered first and then more process related factors. Regarding geometry factors one could think of: (i) a calm zone, (ii) plug flow, (iii) a manifold, (iv) electrode surface properties, (v) the interelectrode distance, and (vi) turbulence promoters.

The inlet to and the outlet from the interelectrode gap can have a pronounced effect on the flow distribution in the reaction space. Calm zones before and after the interelectrode gap reduce this effect and facilitate a more homogeneous flow distribution at the electrodes. Limited residence time for the electrolyte is preferred, because this ensures fresh reactants in the reaction cell, promoting small concentration gradients and a more equal potential distribution across the electrode surface [22].

Plug flow is another effective path to realize uniform electrolyte flow [23]. Plug flow can be achieved by a full width inlet to and outlet from the interelectrode gap. Manifolds can also be used to equalize the flow, but if the manifold ends and starts close to electrode it is likely that the flow profile is influenced by the manifold [24].

The electrode area can be increased by surface roughening or using 3D structures like meshes or foams. A nice side effect is that these options also promote turbulence [21]. Electrodeposition can be used to produce a nanostructured electrode surface [25]. The cost of mesh electrodes can be limited by using a cheap base material sputter-coated with the more expensive catalytic material [26].

The distance between the electrodes increases the resistance for current and ion supply to the electrodes. The gap between electrodes must therefore be reduced as much as possible, but in a way that avoids any surge of current between the electrodes [27]. Note that reducing the gap

increases pressure drop and thus electrolyte pumping cost.

The relative electrolyte velocity can be increased by increasing the electrolyte flow rate, e.g. by pumping the electrolyte in a circulation loop. Though this has a limited effect on the velocity close to the electrode. A turbulence promoter in the interelectrode gap is an alternative. The electrolyte is then forced to flow around the turbulence promoter, e.g. a net, increasing the velocity close to the electrode surface. Turbulence promoters can increase the pressure drop, but the increased mass transport is able to make turbulence promoters favourable [22]. Turbulence promoters are also helpful in enhancing the uniformity of the flow [21].

Caution is advised because turbulence promoters can also reduce the mass transfer. Reasons for this can be: (i) the turbulence promoter blocks part of the electrode and membrane area, (ii) the turbulence promoter diverts the flow forming preferential channels forming a bypass, and (iii) the structure formed by the turbulence promoter leads to flow recirculation and stagnant zones. The effect of turbulence promoters strongly depends on the geometrical features [28]. Main factors affecting the effectiveness seem to be the ratio of filament diameter to the inter-filament distance, the filament diameter and the angle between the filaments. The objective for a turbulence promoter is high wall shear and low pressure drop [29].

The KOH concentration of the electrolyte is a more process related factor. The electrical resistance can be decreased by increasing the KOH concentration. Though for small interelectrode gaps the effect can be limited. A higher KOH concentration also improves reaction kinetics[13].

1.3. Bubble origination and behaviour

In this section the behaviour of gas bubbles in electrolyzers and their effects are studied, and most importantly potential strategies to reduce the negative effects. The next subsection emphasizes the importance of bubble control by listing the effects of bubbles.

1.3.1. The (un)favourable effects of bubbles

Bubbles have both positive and negative effects on the electrolysis.

Positive effects are:

- Bubbles can act as a turbulence promoter. Bubbles push the surrounding liquid during their growth and movement, increasing electrolyte mixing [30].
- Growing bubbles on the electrode surface absorb dissolved gas from the electrolyte and push the electrolyte away, inducing micro mixing in the fluid [31]. It is reported as a positive effect, though an adhering bubble blocks part of the electrode surface.
- Detached bubbles rise in the electrolyte due to the density difference with the electrolyte, inducing macro mixing [31].
- Enhancement of ionic mass transfer to and from the electrode. Bubbles which detach from the electrode cause ions to move towards the electrode, and dissolved gas to transfer to the bulk [32].

Negative effects are:

- Bubbles increase the ohmic resistance between the electrodes resulting in a lower reaction rate or overpotential [33].
- Bubbles can act as a curtain in front of the electrode, forming a resistive film for ions supply heading to the electrode to participate in the reaction [30].

These negative effects are related to resistance both for electrical current and ion supply.

All these effects have to do with improving mixing on different scales.

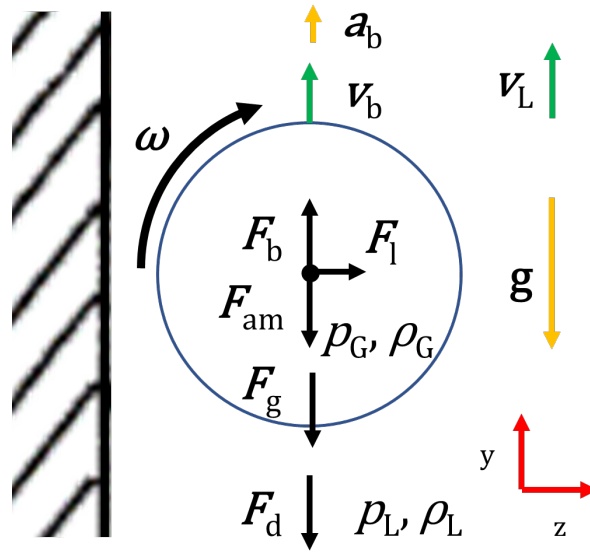


Figure 1.2: A rising, accelerating gas bubble in the flowing electrolyte near a vertical electrode wall with the forces acting on it. With bubble acceleration a_b , bubble velocity v_b , liquid velocity v_L , gravitational acceleration g , angular velocity ω , the pressure inside the bubble p_G , the pressure in the liquid p_L , the density of the gas ρ_G and the density of the liquid ρ_L . The forces acting on the bubble: the buoyancy force F_b , the lift force F_l , the added mass force F_{am} , the gravity F_g and the drag force F_d .

It is thus crucial to manage bubbles well, and take advantage of bubbles if possible. Three factors that determine the creation, size and growth of gas bubbles are surface tension, chemical absorption and the type of gas. Surface tension is a general phenomenon that is not limited to electrolysers. The other phenomena are described below specifically with regard to electrolysers.

1.3.2. Theoretical bubble behaviour

This subsection deals with the theoretical background of bubble behaviour from a force perspective. An overview of the forces acting on a rising, accelerating gas bubble in a liquid is shown in figure 1.2. On a bubble acts buoyancy, gravity and pressure when the bubble has no acceleration, rotation and velocity with respect to the surrounding liquid. The buoyancy force (F_b) is the force as a result of the difference in density between the gas bubble ρ_G and the surrounding liquid ρ_L . The liquid is denser and pushes the bubble upwards. The gravitational force (F_g) is linked to the bubble mass and pulls it down. The pressure acts on the surface of the bubble and is determined by the difference between the gas pressure inside the bubble p_G and the liquid pressure outside the bubble p_L [33, 34].

The drag force (F_d) is only present when the bubble moves relative to the liquid. The drag force is strongly related to the existence of a wake, to the bubble velocity V_B and depends on the shape of the bubble. If the bubble is spherical, the wake and therefore the drag will be limited [33]. The lift force (F_l) is used to account for the rotation induced by the flow field which moves the bubble away from the wall. This force is thus only present when the bubble rotates [35]. Finally, there is the added mass force (F_{am}) which exists only when the bubble accelerates. Added mass is the altered inertia of an object due to the motion of the fluid around the object. It is related to the volume of fluid that has to be displaced so that the bubble can move. [34].

Surface tension is a result of unbalanced attractive intermolecular forces which cause the interface between two immiscible fluids to behave as if it were a stretched membrane under tension. This surface tension causes a pressure difference across curved interfaces. Equation (1.6) shows the relation between the pressure difference and the interface shape. If viscosity effects are negligible equation (1.6) becomes equation (1.7). With \hat{n} the normal vector, \mathbf{T} the stress tensor

in Nm^{-2} , σ the surface tension in Nm^{-1} , R_i the bubble radius in direction i in m, p_G the gas pressure in Nm^{-2} and p_L the liquid pressure in Nm^{-2} [34].

$$\hat{n} \cdot (\mathbf{T}_1 - \mathbf{T}_2) \cdot \hat{n} = \sigma \left(\frac{1}{R_1} + \frac{1}{R_2} \right) \quad (1.6)$$

$$p_G - p_L = \sigma \left(\frac{1}{R_1} + \frac{1}{R_2} \right) \quad (1.7)$$

$$\Delta p = \frac{2\sigma}{R_1} \quad (1.8)$$

In the absence of buoyant forces and fluid motion, a bubble in a liquid will assume a spherical shape since that shape minimizes its surface area. For a spherical bubble $R_1 = R_2$ and equation (1.7) can be rewritten to equation (1.8). For this formula can be seen that if R_1 goes to zero, Δp goes to infinity. And if R_1 goes to infinity, Δp goes to zero. If the bubble contains CO_2 , Δp may cause more CO_2 to dissolve into the catholyte, which causes the bubble to shrink. Δp is even higher in a smaller bubble, and this can cause even more CO_2 to dissolve. So, small bubbles containing CO_2 can be squeezed out of existence by surface tension. A bubble, on the other hand, can also absorb CO_2 if the CO_2 concentration of the catholyte directly surrounding a bubble is high, which is later explained in more detail.

So a significant number of forces acts on the bubbles, and it is relevant to know which forces are dominant. Dimensionless number express the ratio between forces and can therefore be used to determine the dominant force [34].

$$We = \frac{2rv_B^2\rho_L}{\sigma} \quad (1.9)$$

$$Bo = \frac{4r^2g(\rho_L - \rho_G)}{\sigma} \quad (1.10)$$

$$Ca = \frac{\mu_L|v_B|}{\sigma} \quad (1.11)$$

$$Re_B = \frac{d_B|v_B|\rho_L}{\mu_L} \quad (1.12)$$

$$Fr' = \sqrt{\frac{u_B^2\rho_L}{2r(\rho_L - \rho_G)g}} \quad (1.13)$$

The Weber number (equation 1.9) indicates the ratio of inertia over surface tension force. r is the bubble radius in m, v_B is the bubble velocity in ms^{-1} and ρ_L the electrolyte density in kgm^{-3} . Bubbles are easily deformed by fluid acceleration at high We . We is below one for bubble radius up to 0.004 m and bubble velocities up to 0.2ms^{-1} , so surface tension is dominant over inertia. Therefore, the bubbles are probably nicely spherical.

The Bond number (equation 1.10) is the ratio of gravity over surface tension force. g is the gravitational acceleration is ms^{-2} and ρ_G is the gas density in kgm^{-3} . It increases quadratic with bubble diameter and is independent on bubble velocity. Bo remains below one for bubble radius up to 0.001 m. As this small bubble radii are expected, surface tension will be dominant over gravity [3, 31].

The Capillary number (equation 1.11) indicates the viscous stress over surface tension stress, with μ_L is the dynamic viscosity of the electrolyte in $\text{kgm}^{-1}\text{s}^{-1}$. The viscous stress depends on the 'stickiness' of a fluid, it is a measure of the resistance to flow. Ca increases linearly with bubble velocity and is independent on bubble size. Ca is almost zero for bubble velocities up to 2ms^{-1} , so surface tension is dominant over viscous effects.

Two other well known dimensionless quantities are the Reynolds number (Re) and the Froude number (Fr). These numbers provide also some information about the bubble behaviour. Re indicating the ratio between inertia and viscous forces, is represented by equation (1.12) for a rising gas bubble in a liquid, with d_B the bubble diameter in m. For the bubbles inside the flow channel $2 < Re < 300$, so inertia is dominant. Fr (equation 1.13) is the ratio of inertia over buoyancy force. The inertia force is determined by the bubble velocity. Fr is below one for bubble radius up to 0.004 m and bubble velocities up to 0.06 ms^{-1} . Buoyancy is thus dominant over inertia.

The conclusion of this force discussion is that surface tension plays an important role in the bubble behaviour. At the end of this section is discussed how this can be used for bubble mitigation.

1.3.3. Formation and development

Bubbles in electrolyzers form as a result of supersaturation [30]. The electrolyte can become supersaturated due to pressure drop. The condition for this is that the solubility of the gas decreases with pressure decrease. The production of dissolved gas as a result of the electrolysis reaction is another reason for supersaturation. Figure 1.3 summarizes all the potential gas behaviour in a supersaturated electrolyte.

Dissolved gas is produced as a result of the applied current at the electrodes. So the dissolved gas concentration is the highest at the electrode surface and decreases towards the bulk region. The supersaturation of dissolved gas remains limited and no bubbles are formed as a result of the electrical current if the current density is low [36]. When the current density increases, and the interfacial concentration exceeds a certain value, nuclei at the electrode surface become active and dissolved gas is transformed into the gaseous phase. The concentration at which nucleation starts, depends on the properties of the electrolyte, the gas, and the surface morphology of the electrode. Note that only a fraction of the dissolved gas is transformed into bubbles [37].

Bubbles grow by adsorbing dissolved gas from the surrounding electrolyte [30, 31]. Bubbles can either slide along or detach from the electrode as shown in figure 1.3a. A sliding bubble can still absorb dissolved gas, and it can collide with other attached bubbles. Grown bubbles leave the electrode surface depending on the surface conditions, angle of contact between the bubble and electrode, properties of the electrolyte, electrolyte velocity, dissolved gas concentration, current density and cell voltage [38]. When the bubble moves away from its nucleation site, at that spot a new bubble is formed. Sliding bubbles leave behind a bubble-free track on the electrode surface. Thereafter, on these tracks a burst occurs of freshly formed bubbles [39].

Bubbles in aqueous solutions tend to accumulate surface-active contaminants at their gas-liquid interface. The interface can become immovable if the concentration of these contaminants is large enough. This can have a pronounced effect on the bubbles in an electrolyzer, because it has been shown above that We is very low and surface tension is highly dominant over inertia. The result is that bubbles can behave like rigid spheres which might cause problems when moving through and out of the cell [40].

1.3.4. Behaviour in the bulk

This section discusses the bubble properties and behaviour in the bulk. After nucleation and detachment the bulk consists of a two phase flow with bubbles of different sizes. In the bulk the dissolved gas can be absorbed in the bubbles present or exit with the electrolyte [37], see figure 1.3a. Note that the electrolyte also can be dissolved in a gas bubble [41].

In the discussion on dimensionless numbers was shown that size influences the hydrodynamic behaviour, and in the part on nucleation the detach diameter was already discussed. Logic factors influencing the bubble size in the bulk are detach diameter and growth, but there are also other factors. The following are stated: breakup and coalescence [30], the nature of electrolyte [31], pressure [42], current density [43], number of nucleation sites, surface wettability [3] and

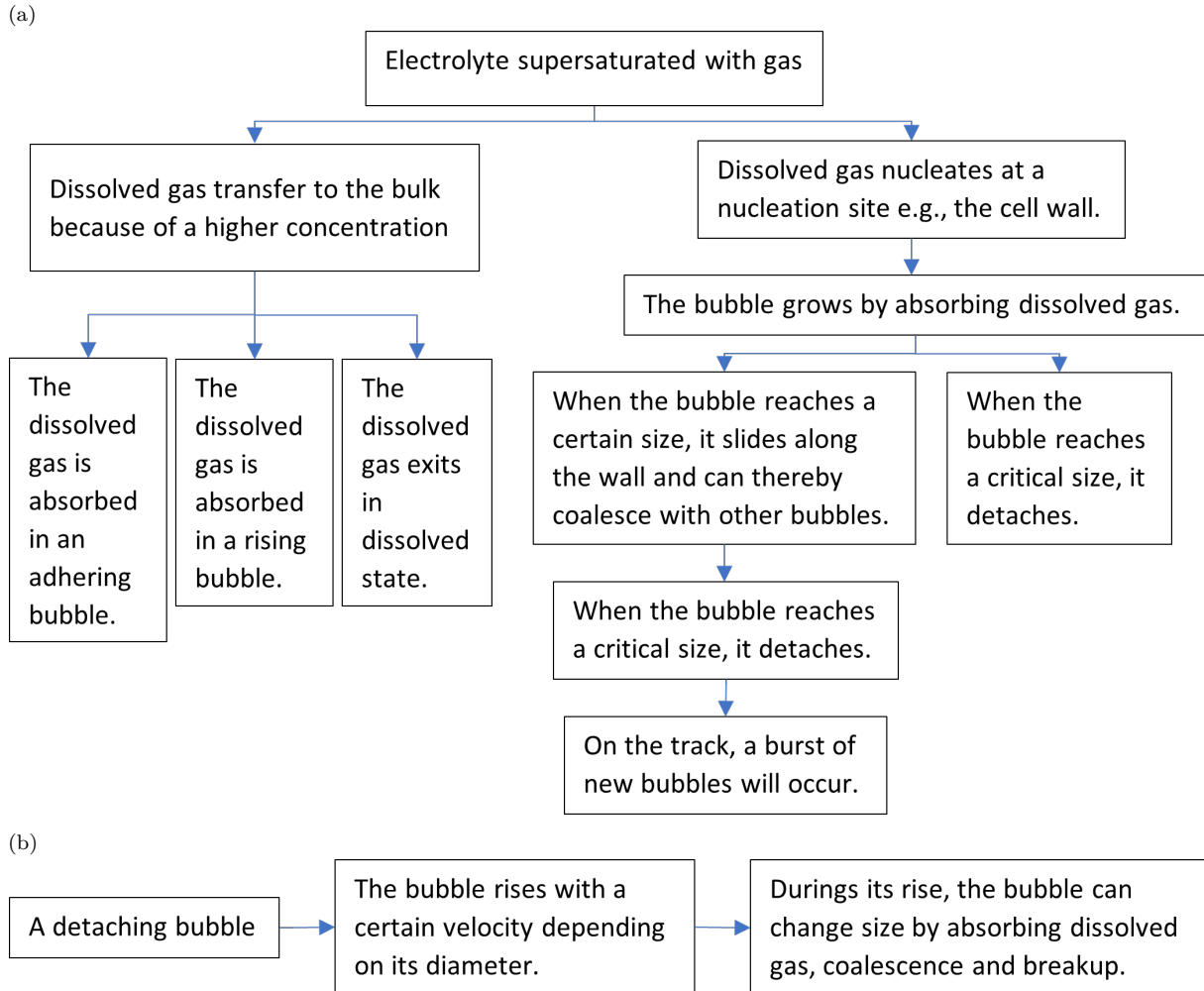


Figure 1.3: Processes of the formation and movement of bubbles. (a) Supersaturation is the prerequisite for bubble nucleation. If there is locally supersaturation, the dissolved gas can either transfer to the bulk or nucleate on the cell surface. This scheme shows the possible routes for dissolved gas. (b) When a bubble detaches from the cell surface, it will rise in the electrolyte. The bubble velocity with respect to the electrolyte depends on its diameter. A detached bubble can still grow by absorbing dissolved gas or by coalescing with other bubbles.

electrolyte velocity [38].

The bubbles are smaller at higher pressure. For water electrolysis applies that the majority of cathodes produce $5 < d < 20 \times 10^{-5} \text{ m}$ H_2 bubbles at atmospheric pressure [3, 31]. Small bubbles are entrained with the flow, so the velocity is zero relative to the electrolyte. It is stated that the vertical velocity relative to the electrolyte of electrolytically generated bubbles is negligibly small [44].

Collision, the cause of coalescence, can occur by three mechanisms: (i) turbulent fluctuation of the liquid phase, (ii) laminar shear, and (iii) different rising velocities. The latter is a result of the difference in bubble size. The most predominant of these three is turbulence, it induces both coalescence and breakage of bubbles [31].

The type of gas influences the bubble behaviour too. H_2 bubbles grow faster than O_2 bubbles in a membrane-less water electrolyser. O_2 bubbles have larger coalescence tendency than H_2 bubbles. This might be one of the reasons that H_2 bubbles are smaller than O_2 bubbles. Consequently, H_2 bubbles sliding along the electrode do not swallow up attached bubbles as easily as O_2 bubbles do, due to the different coalescence behaviour. Experiments showed the existence of a layer of free H_2 bubbles, gliding over the layer of attached H_2 bubbles. The layer of the gliding bubbles hardly affected that of the attached bubbles. At the anode such a phenomenon has not been

observed [33, 39].

Bubbles influence the electrolysis and therefore the efficiency too. The electrical resistance varies over the height of the cell due to the increasing amount of bubbles towards the top. The relative resistivity of the interelectrode gap depends on three dimensionless parameters: (i) the ratio of liquid to gas flow rates, (ii) the thickness of the stagnant bubble layer(s), and (iii) the relative resistivity of the bubble layer. With a cell to be operated at a constant load the electrolyte flow rate and the interelectrode gap are the most important variables [44, 45]

The shielding factor, understood as the fraction of the electrode surface which is shadowed by adhering bubbles in orthogonal projection, is closely linked with the bubble population density. This factor depends not only on the current density but also—substantially—on the surface properties of the electrode. The shielding factor controls the extent of the microflow and its strength [43].

Zero-gap cells have no ohmic resistance between the membrane and the electrode, because there is no distance between the membrane and electrode. These cells are thus not affected by the resistance to electrical current and ion supply caused by bubbles in the interelectrode gap. The bubbles are forced to leave from the back of the porous electrode. Also for this configuration applies that the electrolyte flow helps to detach the bubbles from the electrode surface [46].

There are porous electrodes designed that help with the detachment of bubbles. For example, electrodes were developed with small pores on the membrane side and wider pores on the other side, for easy bubble removal [47]. The zero-gap design brings some challenges, the gas removal must be effective to avoid problems, and reducing the capital cost as the membranes and electrocatalysts are expensive [48]. As a result, the technology was not yet mature in 2016 and there have been no breakthroughs for CO₂ electrolysis in recent years.

1.3.5. Mitigation

From the above it can be concluded that several things can be done to manage the gas bubbles. The measures can be divided into three categories: (i) cell geometry, (ii) material properties and (iii) operating conditions.

For cell geometry the main recommendation is to reduce the interelectrode gap to limit the electrical resistance [13]. The optimum gap depends on the current density and the height of the electrodes [49]. It is recommended to keep the height limited for gas evolving electrodes, because of the increasing void fraction towards the top. Pressure drop is another reason to limit the height. Cells with different aspect ratios were studied, but no conclusion was drawn about the best ratio between height and width of the cell [22, 50].

Surface and electrolyte properties influence the formation and development of bubbles. Bubbles nucleate on surfaces in the cell, these surfaces can be treated to change the nucleation [51]. Alternatively the electrolyte properties can be changed by adding a surfactant [52]. Care must be taken regarding the quality of the dissolved gasses in the catholyte. If the CO₂ feed, for example from flue gas, contains surface-active contaminants, it can negatively influence the bubble behaviour.

Regarding the operation conditions the electrolyte velocity and current density are important. The velocity should be sufficiently high: (i) to keep the gas fraction low and, correspondingly ohmic voltage drop [53], (ii) to prevent secondary chemical reaction [44], (iii) to prevent the dissolved gas from nucleation, and (iv) to keep the detach diameter of bubbles low [54].

The engineering task is to design an electrolyte velocity large enough to get an acceptable voltage drop and small enough to get moderate expenditure of pumping energy (or—with electrolyte self-circulation—of piping investment) [44].

Current density influences if the electrode is a gas evolving one, how much gas is evolved and the bubble size [32, 37]. It effects also whether macro or micro convective mass transfer is dominant. An increase in macroconvection decreases the microconvective effects that feed the growth of a

bubble. Macroconvection also ‘steepens’ the concentration gradient from the electrode surface to the bulk. This results in a smaller region of highly concentrated, dissolved gas with which to feed the growing bubble. Low current densities leave the flow laminar, but when the current density is increased it can become turbulent [31].

1.3.6. Design guidelines

Bubble formation and behaviour depends on a lot of factors, like electrode and electrolyte properties, current density, pressure and electrolyte velocity (influencing supersaturation and bubble size). From the dimensionless numbers can be concluded that surface tension is dominant over inertia, gravity and viscous stress. When it comes to cell design, the gap should be kept small and the height limited.

1.4. Approach of this study

The research so far does not provide ready-made solutions to the challenges facing Coval. So the question to be answered is: How can the current knowledge of electrolyzers be applied to improve the Coval electrolyser design regarding flow distribution and mitigation of the impact of dissolved gas production?

The flow distribution in the reactor was already studied by Jos van der Maas, but little is known about bubble behaviour in the reactor. To mitigate the impact of dissolved gas production, a first step is to better understand the nucleation and behaviour of bubbles in the reactor. So the bubble behaviour in the reactor is studied experimentally. A next step is to put the design guidelines and experimental results together to come up with an improved design. Coval wants to be able to assess individual adjustments compared to the present design, therefore a number of concept designs are designed.

To test all these concepts in the lab would be a time-consuming and expensive process. Thus the concept designs are initially assessed using computational fluid dynamics (CFD), this is a numerical tool which allows solving flow conditions in defined geometries. CFD is used successfully and widely to study flow distribution in electrolyzers [3, 24]. After this assessment, the concept designs are improved where necessary and the best adjustments combined, followed by a second CFD assessment. Bubble behaviour and flow distribution in the potential designs is experimentally investigated. Finally, prototypes are produced to be tested in the high pressure electrolyser.

The optimized design has to meet the following requirements:

- Homogeneous flow distribution over the all the interelectrode gaps of the stack and within each interelectrode gap. For proper operation equal electrolyte distribution over all the reaction surface available is important, see section 1.2 and figure 1.4.
- The adjustments to the design must be able to be tested in the existing CO₂ electrolyser setup, so the maximum width of the flow channel 0.108 m and the maximum length is 0.125 m. This allows for fast and cheap assessment of a new design.
- Accumulation of gas in the cell must be avoided, because this has negative effects on the electrolysis see section 1.3.1.
- Mature technology, as Coval wants to commercialize it, it is preferred that the design is reliable and based on proven techniques.

The focus of this research is on achieving a better performing design, the experiments, tests and the CFD model are tools in this. It is important for Coval that the effects of the various adjustments to the present design is clear.

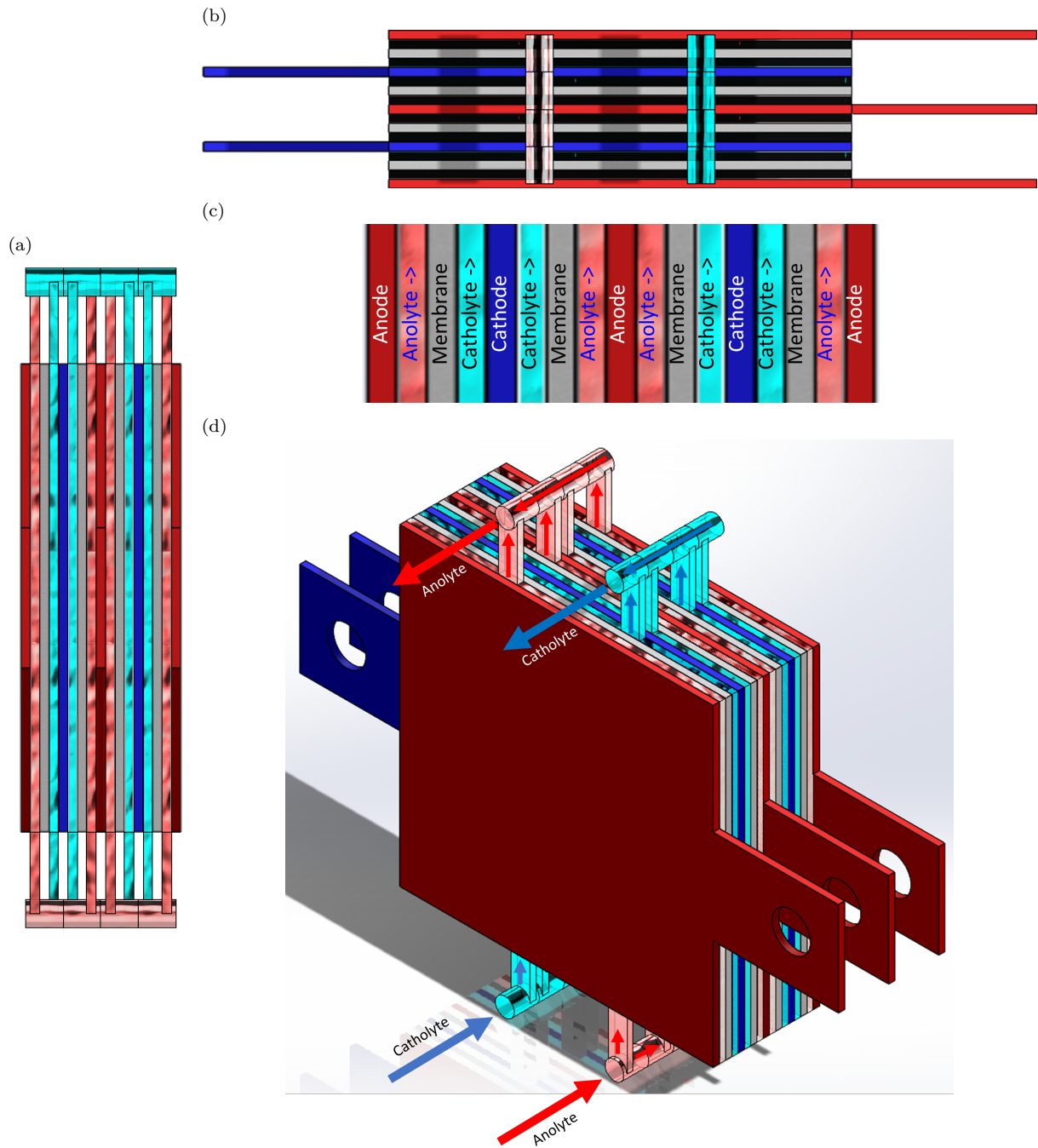


Figure 1.4: Simplified representation of the present electrolyser stack, the electrolyte flows from bottom to top. The solid red and solid blue plates are the anode and cathode respectively, the solid grey sheets are the membranes. The dimensions of the active area are 0.01 m^2 . (a) Side view, the height of the assembly is 0.141 m , (b) top view, (c) detail of the layers in 1.4a, and (d) isometric view of the stack with the streams indicated.

2. Numerical methodology

This chapter and chapter 3 give more detailed information on how the main question of this thesis project is answered. This chapter describes how the CFD model is set up, which is used in two rounds. In the first round, the model is used to screen individual adjustments to the present design. In the second round, combined adjustments are screened. Finally, the CFD results are used to select prototypes to be experimentally tested.

The desired flow in the inter electrode gap is an ideal plug flow in vertical direction. So when the flow front is like a horizontal plane moving upwards in vertical direction. See also figure 2.1 and image the fluid going from the green, to the blue and the red level successively and having no velocity in horizontal direction. In that case each fluid 'package' has the same residence time in the inter electrode area.

2.1. Assumptions

CFD is a numerical tool which allows solving flow conditions in defined geometries. In this case CFD was used to obtain data about velocity and pressure in geometries like presented in figure 1.1. The following assumptions were made in the model: (i) steady state, (ii) temperature and viscosity are constant, (iii) incompressible and (iv) laminar flow. The last assumption holds, because the Reynolds numbers are below 2300, according to White [55]. The Reynolds numbers in the inlet and outlet pipes to and from the square cell are calculated with equation (2.1). For the Reynolds number inside the cell and the rectangular inlet and outlet the hydraulic diameter is used as defined by White [55], resulting in equation (2.2). \dot{V} is the flow rate in m^3s^{-1} , ρ is the liquid density in kgm^{-3} , r is the pipe radius in m , μ is the dynamic viscosity in $\text{kgm}^{-1}\text{s}^{-1}$, h is the channel height in m and w is the channel width in m .

$$Re = \frac{2\dot{V}\rho}{r\pi\mu} \quad (2.1)$$

$$Re_{D_h} = \frac{2\dot{V}\rho}{(h+w)\mu} \quad (2.2)$$

2.2. Governing equations

The governing equations are mass and momentum conservation, equation (2.3) and equation (2.4). These equations determine the Ansys Fluent solver settings. \mathbf{u} is the velocity vector in ms^{-1} and f is the body force in Nm^{-3} .

$$\nabla \cdot \mathbf{u} = 0 \quad (2.3)$$

$$\rho \mathbf{u} \cdot \nabla \mathbf{u} = -\nabla p + \mu \nabla^2 \mathbf{u} + \mathbf{f} \quad (2.4)$$

$$w(r) = \left(-\frac{dp}{dz} \right) \frac{R^2 - r^2}{4\mu} \quad (2.5)$$

$$w(x,y) = \frac{2\dot{V}}{R^2\pi} \left(1 - \frac{(x-b)^2 + (y-c)^2}{r^2} \right) \quad (2.6)$$

For all the walls, so both of the inlet and outlet pipes and the reactor cell, a no slip boundary condition is applied. A laminar velocity profile is prescribed at the entrance of the inlet pipe



Figure 2.1: The flow domain between the electrode and the membrane. The electrolyte enters the interelectrode gap perpendicular to the sheet through the hole at the bottom. Next, the electrolyte flow upwards through the gap. Finally, the electrolyte leaves the gap through the hole at the top perpendicular to the sheet. A plug flow is desired in this domain, so a flow front like a horizontal plane moving purely upwards. One could imagine the fluid going from the green, to the blue and the red line successively and having no velocity in horizontal direction. In that case each fluid 'package' has the same residence time in the inter electrode area. The interelectrode gap is 0.1 m wide.

Table 2.1: Overview of key parameters of the CFD simulations

Property	Value
Density	998 kg m^{-3}
Dynamic viscosity	$0.001002 \text{ kg m}^{-1} \text{ s}^{-1}$
Gravitational constant	9.81 ms^{-2}
Inlet boundary condition	equation (2.6)
Outlet boundary condition	1.01325 Pa
Flow rate	20 h^{-1}

(equation 2.6), based on the Hagen-Poiseuille flow (equation 2.5). This function is a paraboloid at the inlet surface, concentric with the inlet pipe. In equation (2.6) the general form of the Hagen-Poiseuille flow is rewritten to Cartesian coordinates and based on the flow rate. With the flow rate \dot{V} in $\text{m}^3 \text{ s}^{-1}$, inlet pipe radius R in m, the x coordinate of the inlet b in m, the y coordinate of the inlet c in mand $0 \leq r \leq R$. The outlet boundary is defined as a pressure outlet at atmospheric pressure.

SIMPLE was chosen for the pressure-velocity coupling, because a steady state simulation is carried out, according to [56]. Fluent was set with double precision and a pressure-based solver, which is the default for incompressible flows. Second order was chosen for the pressure interpolation scheme, and second order upwind for momentum, which is the default. The simulation parameters are summarized in table 2.1. A relatively high flow rate was chosen, because previous research by Jos van der Maas showed that the flow distribution was highly uneven especially at higher flow rates. The flow distribution tend to be more homogeneous at lower flow rates [7].

2.3. Geometry and mesh

It must be ensured that the flow in the cell is independent of the inlet and outlet pipe to study only the flow effects inside a single cell. This means that the flow needs to be fully developed at the cell entrance and at the exit of the outlet pipe. For the inlet this can be obtained by prescribing a velocity profile. In case of the outlet, it is made sure that the flow is fully developed inside the outlet pipe. For a fully developed flow the outlet pipe needs to have a length of at least L_e (equation 2.7) [55]. With \dot{V} the flow rate in $\text{m}^3 \text{ s}^{-1}$, ρ the fluid density in kg m^{-3} and μ the dynamic viscosity in $\text{kg m}^{-1} \text{ s}^{-1}$. After running the simulations it was determined that 0.02m inlet pipe is required, to adjust for the upstream effects.

$$L_e \approx \frac{0.24\dot{V}\rho}{\pi\mu} \quad (2.7)$$

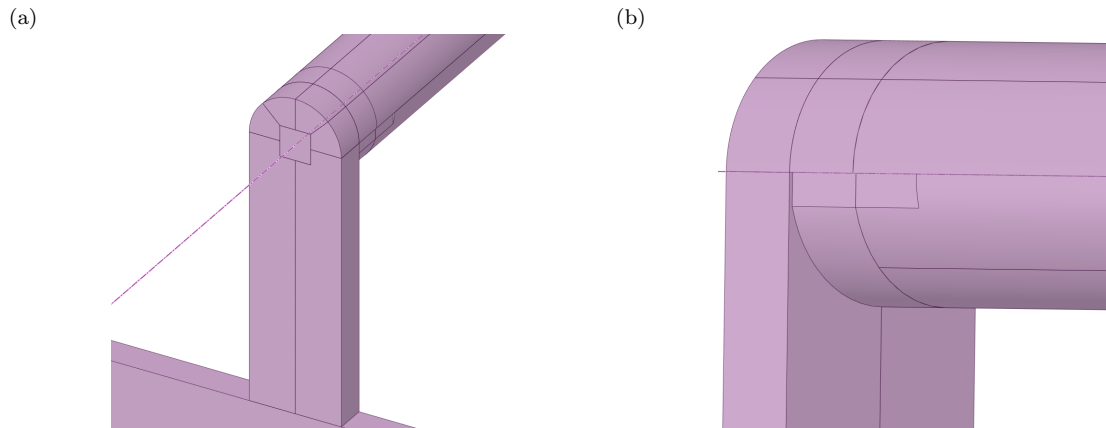


Figure 2.2: Detail of the top part of the conventional cell with the outlet pipe and its connection to the square cell. The cell has a thickness of 2 mm and the outlet pipe a diameter of 6 mm. (a) Chopped geometry to guide the mesher. (b) The circumference of the pipe is adjusted to avoid a cusp.

The next step after defining the geometry is building a mesh. Adjustments to the geometry were made to guide the mesher in creating a grid with low skewness. These adjustments involve chopping and avoiding cusps as shown in figure 2.2. The mesh dependence of the solution is assessed by printing the mesh on the solution and checking whether imprints of the mesh are visible. Convergence is judged by looking at the convergence of the friction factor.

3. Experimental methodology

Experiments have been conducted to study: (i) the fluid dynamics further, (ii) the gas behaviour, and (iii) the high pressure electrolyser outflow regarding bubbles. This chapter describes the methodology for this three types of experiments. In chapter 5 the results of the experiments are discussed.

3.1. Bubble visualization in the high pressure reactor

The high pressure electrolyser is a visually closed system, which makes it hard to study the bubble behaviour, if there are any bubbles. The hypothesis is that bubbles are formed. At the cathode side two gasses possibly nucleate, namely CO_2 and H_2 . CO_2 bubbles can form as a result of pressure drop in the with CO_2 saturated catholyte. Also the acid conditions near the bipolar membrane can induce CO_2 nucleation. H_2 bubbles can form when there is locally a lack of CO_2 . At the anode side the expected bubbles are O_2 bubbles, produced by the electrolysis reaction. Till now this is only a hypothesis, the gas bubbles were never studied before. So, there is no information about the presence and the type of gas bubbles in the system.

The setup to study the reactor outflow is graphically presented in figure 3.1. Two sight glasses of the following type were used to visualize the flow: Noris sight flow indicator, Bauform 881, Body: 1.4408, Soda Lime glass DIN 8902, Gasket: graphite, G 1/2" / PN 40, NPT thread

In this experiment the influence of current density, flow rate and pressure on the bubble nucleation are studied. The goal of this experiment is to visually assess the reactor outflow concerning bubbles. The current density, flow rate and pressure will be varied separately and the sensitivity of these parameters on the bubble nucleation estimated.

Procedure

The procedure consist of seven different sub-experiments, which are shown in the table 3.1. All the experiments were ran with CO_2 except for experiment 7. It is necessary to wait until the system is in steady state after each change of a setting. The waiting time is 60 min when changing the pressure and for any other change 30 min. When steady state is reached only a picture is taken if just liquid is visible, when bubbles are present the flow is also recorded for 30s. The image material is used to estimate qualitatively the gas fraction and bubble size distribution.

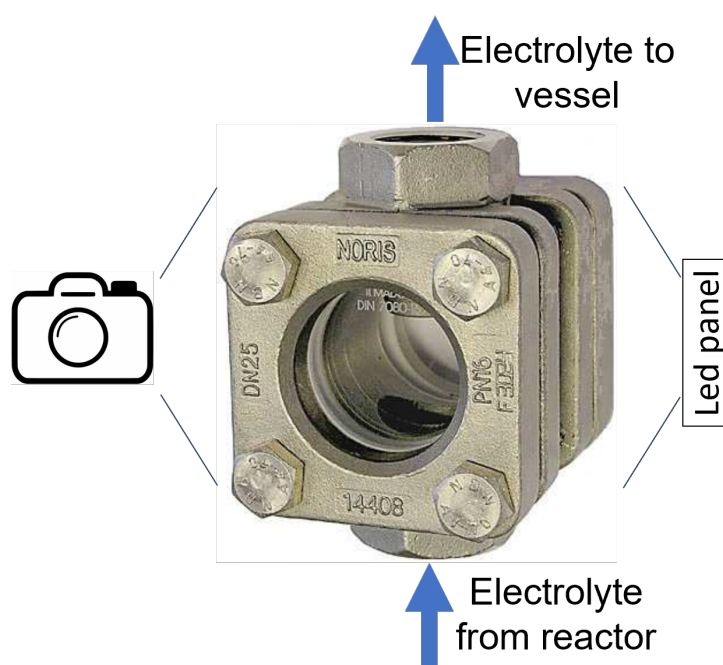


Figure 3.1: The setup to visualize bubbles and to capture the high pressure reactor outflow. The see-through diameter is 32 mm

Table 3.1: Settings for the experiments with the high pressure electrolyser. Experiment 1 to 6 were ran with CO₂.

Experiment	Flow rate (lh ⁻¹)	Pressure (bar)	Current (A)	Voltage (V)
1	8	1	-	-
	8	20	-	-
	8	40	-	-
2	4	40	-	-
	8	40	-	-
	12	40	-	-
	16	40	-	-
	20	40	-	-
3	8	40	1.5	3.5
4	8	40	0	5
	8	40	1	3.5
	8	40	2.5	3.8
	8	40	1	3.5
	8	40	0.8	3.5
	8	40	0.6	3.5
	8	40	0.4	3.5
	8	40	0.2	3.5
	8	40	0	5
5	2	40	1.5	3.5
	4	40	1.5	3.5
	12	40	1.5	3.5
	20	40	1.5	3.5
	12	40	1.5	3.5
	8	40	1.5	3.5
	6	40	1.5	3.5
	4	40	1.5	3.5
	2	40	1.5	3.5
6	8	1	1.5	3.5
	8	20	1.5	3.5
	8	40	1.5	3.5
	8	20	1.5	3.5
	8	1	1.5	3.5
7 No CO ₂	8	40	0.2	3.5
	8	40	0.6	3.5
	8	40	1	3.5
	8	40	2.5	3.8
	8	40	1	3.5
	8	40	0.6	3.5
	8	40	0.2	3.5
	4	40	1.5	3.5
	12	40	1.5	3.5
	20	40	1.5	3.5
	12	40	1.5	3.5
	4	40	1.5	3.5

3.2. Flow visualization cell

Visualizing the reactor outflow does not provide information about the flow distribution and bubble behaviour inside the reactor. A visualisation cell with two transparent sides is used to assess the liquid and gas behaviour inside the reaction cell. The same visualisation cell is used to assess both flow distribution and bubble behaviour. Figure 3.2 shows the experimental setup. The desired result for the flow distribution experiments is an ink front moving purely horizontally upwards in the cell. That means that all fluid follows a similar path through the interelectrode gap, having a similar residence time and a purely vertical velocity.

Materials

The required materials are:

- Camera, including tripod/frame (The camera used was a Ricoh PENTAX K-3)
- Visualization cell
- Spacers or 3D prints of the respective designs.
- Net 0.7 mm thickness
- LED panel
- Indigo carmine solution (3.4×10^{-4} kg per kg solution)
- Pump for liquid adjustable flow rate between 4 and 8 l h^{-1}
- Pump for air with flow rate around 0.1 l h^{-1}

Procedure

The procedure to experimentally assess the flow distribution and bubble behaviour in the visualisation cell:

Flow distribution

1. Prepare the visualisation cell for the design to be tested
2. Pump demineralized water at the flow rate of interest until reaching steady outflow for 3 s
3. Start the recording
4. Simultaneously close valve 1 and open valve 2, see figure 3.2
5. Wait until the cell is filled with indigo carmine (typically 30 to 120 s)
6. Start a new recording
7. Simultaneously open valve 1 and valve 2, see figure 3.2
8. Wait until all indigo carmine has disappeared from the cell and clear water flows out of the exit (typically 30 to 120 s)
9. Stop the recording

Bubble behaviour

1. Prepare the visualisation cell for the design to be tested
2. Pump the indigo carmine solution solution and air for 5 min through the cell
3. Record the flow for 1 min

Processing

Processing of the recordings was necessary to quantify the experimental results. For the flow distribution, plots of the time at which the tracer arrived at a certain cell location were made.

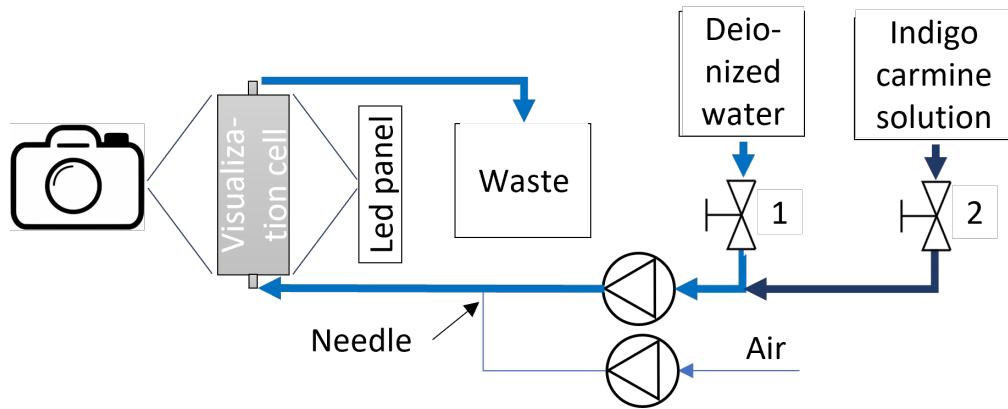


Figure 3.2: Flow visualization setup which allows to study both flow distribution and gas bubble behaviour. The see-through area of the visualisation cell is 0.01 m^2 . Flow distribution is studied using deionized water and an indigo carmine solution. Bubble behaviour can be studied using the indigo carmine solution and the air pump.

For the bubble experiments the gas fraction in the cell over time is determined. The first step in processing is cropping the videos to the area of interest, i.e. the cell area. FFmpeg, a tool for converting video and audio, is used for this. Secondly, FFmpeg was used to create PNG-files from the recordings (10 per second).

The PNG-files were the input for a Python script applied to continue the processing. In the script an array was build with x and y position and time on the axes. Each array element contains a value for the intensity. For the flow distribution, the intensity was used to determine the time when the tracer arrives at the particular location. When a certain intensity drop was seen, the tracer was considered to be arrived at that location. For all the coordinates these times were collected and represented in a contour plot. For optimal cell use, the contours vary only in y direction and not in x direction (over the cell width). In that case each fluid 'package' has the same residence time in the interelectrode gap.

For the gas bubbles a similar approach is applied. Based on intensity is determined for each pixel whether the solution or an bubble is located there. From this data the average bubble fraction is derived and the bubble fraction in time is plotted.

4. Screening of designs with CFD modelling

This chapter first describes the design ideas after which an assessment with CFD follows.

4.1. List of screened adjustments

The starting point for all adjustments is a design with a calm zone, presented in figure 4.1b. This calm zone is chosen to study adjustments less dependent on the inflow. A previous study showed that the flow distribution in the present design (figure 4.1a) is highly influenced by the cell inlet geometry, creating a jet effect, see figure 5.1 [7]. The calm zone can be divided in three parts in the flow direction (bottom to top): (i) proportional division of the entering fluid, (ii) distribution of the fluid to the full cell width, and (iii) the actual calm zone of the same width as the cell.

The adjustments studied in the first screening are:

- a. Calm zone, 0.5 mm cell thickness
- b. Calm zone, 1 mm cell thickness
- c. Calm zone, 2 mm cell thickness
- d. 7 channels
- e. 15 channels
- f. 28 channels
- g. Doubled cross sectional area of the inlet and outlet pipe
- h. Tripled cross sectional area of the inlet and outlet pipe
- i. A constriction in the calm zone
- j. Aspect ration of 0.8
- k. Aspect ration of 1.7

Designs a-c were screened to study the effect of cell thickness on fluid dynamics. Reducing the interelectrode gap is expected to have a positive effect on the ohmic resistance. The model assessed the effect of this change on a fluid dynamical level. Designs c, d-f were simulated to evaluate the effect of (the number of) channels. Channels both increase the electrode area and reduce locally the interelectrode gap, see figure 4.1c.

The modelling results of c, g, h were used to investigate the effect of the size of the inlet pipe. The pipe size is an important factor when the cell is used in a stacked configuration. A low pressure drop in the pipes compared to the cell is required for successful stacking. Design c and i were compared to check the effect of a constriction in the calm zone, see figure 4.1d. The hypothesis is that the constriction will promote equal fluid distribution over the cell width, with the benefits and not the burdens of a manifold.

And finally, a comparison was made between c, j and k to assess the effect of different aspect ratio, i.e. the ratio of the height over the width. Varying the aspect ratio changes the cross section of the flow channel inside the cell, and therefore also the relation between flow rate and flow velocity, and the pressure drop inside the cell.

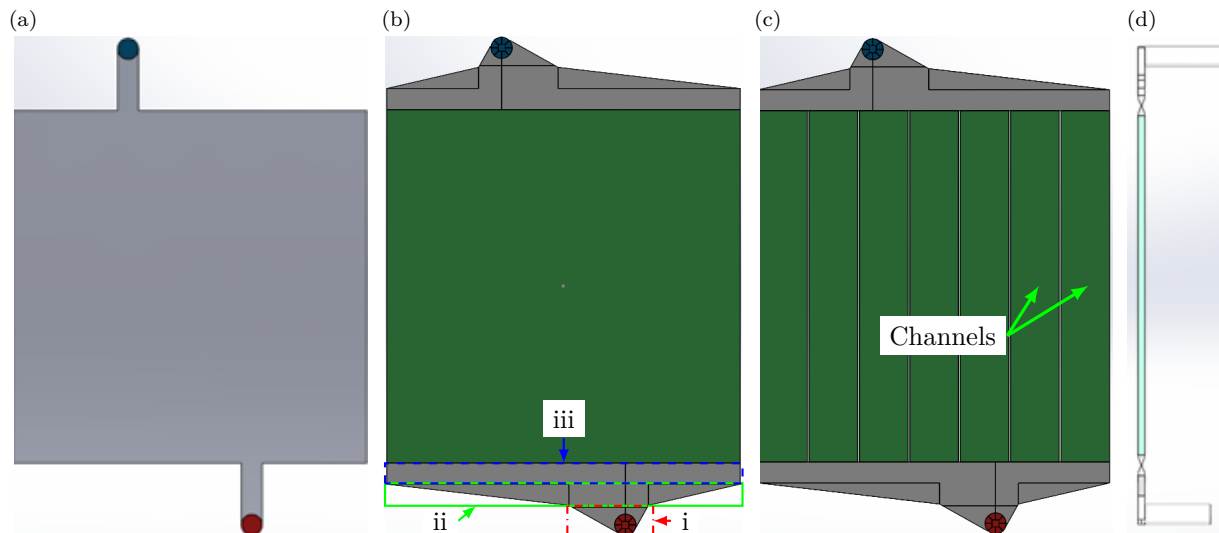


Figure 4.1: Several designs screened with CFD. The red and the blue circles at the bottom and top represent the inlet and outlet respectively, both perpendicular to the cell. All these cells have a width of 100 mm and an inlet and outlet pipe diameter of 6 mm. (a) The present design. (b) The design with a calm zone at the entrance and exit of the cell. The calm zone can be divided in three parts in the flow direction (bottom to top): (i) proportional division of the entering fluid, (ii) distribution of the fluid to the full cell width, and (iii) the actual calm zone of the same width as the cell. (c) A design with channels to guide flow. (d) A side view of a design with constrictions at the beginning and end of the cell to promote equal flow distribution over the cell width.

4.2. First CFD screening

The CFD model provides information about velocity in the flow domain and enables to assess to what extent ideal plug flow is achieved with a certain adjustment to the design. For ease of comparison between the CFD results obtained for each design, velocity graphs are derived from the velocity contours, 4.2b. Figure 4.5c shows the vertical velocity distribution at the green, blue and red level, presented in figure 4.2a.

For the rest of this section, we focus on the velocity at the green level, i.e. at $y = -0.044$ m. This location is chosen for two reasons. Firstly, the CFD result at $y = 0$ m for the velocity is similar for all modelled designs, and therefore not useful for comparison. Secondly, the plug flow profile is desired from bottom to top, so this location should be included in the assessment. The top velocity profile (red level) is similar to the bottom profile (green level) for all design, thus only the velocity at $y = -0.044$ m is considered.

Figure 4.3 shows the effect of several parameter on the flow distribution, namely the number of channels (figure 4.3.a), the cross sectional area (figure 4.3.b), the thickness (figure 4.3.c) and aspect ratio (figure 4.3.d). The incorporation of channels make the flow more homogeneous, (figure 4.3.a). The difference between the extreme values marked in the plot becomes less extreme (0.016 m s^{-1}) compared to an empty inter electrode gap (0.051 m s^{-1}). Nevertheless, there is no clear difference for flow velocity when the number of channels is varied.

Doubling the cross sectional area of the inlet and outlet pipes and a constriction, show a similar improvement, figure 4.3.b. Tripling the cross sectional area on the other hand does not improve significantly the velocity distribution. Both a constriction and larger pipes do not bring as much improvement as the channels.

All simulations were ran for the same flow rate, so one could expect that the velocity graphs in figure 4.3.b should have the same average velocity. This is not the case for two reasons. Firstly, only the vertical velocity component at $z = 0$ m is shown, so no conclusion can be drawn about conservation of mass based on this data alone. Secondly, the flow cannot be described as a fully developed Poiseuille flow between parallel plates.

The major effect of changing the cell thickness is that the magnitude of the velocity increases

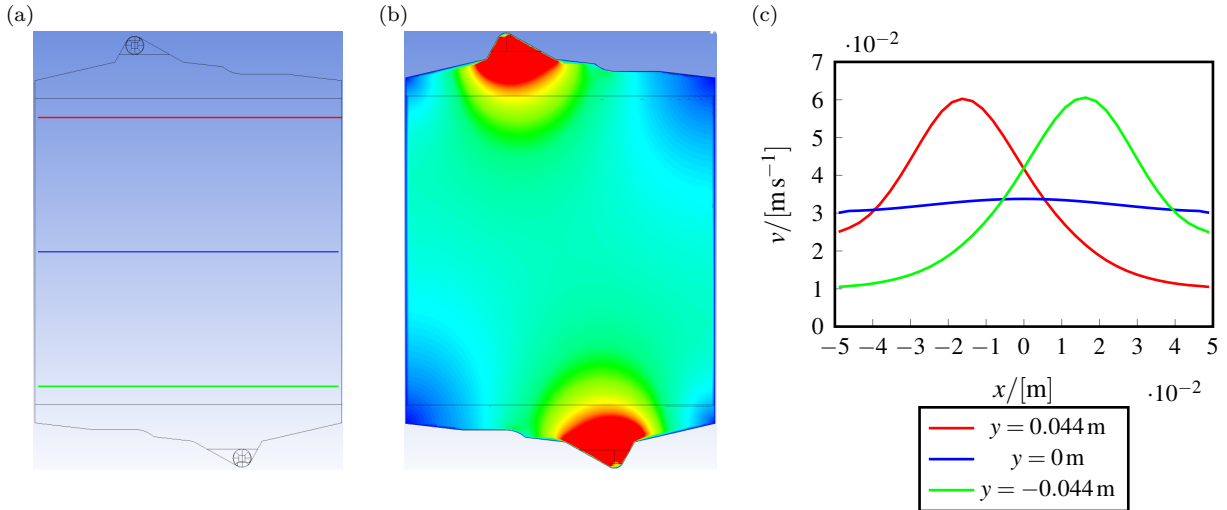


Figure 4.2: The velocity at various locations in the cell for the calm zone design with 2 mm cell thickness. (a) The locations of the velocity measurements: green ($y = -0.044\text{ m}$), blue ($y = 0\text{ m}$) and red ($y = 0.044\text{ m}$). (b) The velocity in contours in the cell at $z = 0\text{ m}$ (the middle plane). (c) The vertical velocity over the cell width (0.1 m) at the three locations.

over the full cell width, figure 4.3.c. Reducing the cell thickness increases the absolute difference between the velocity maxima and minima. This makes the variation in cell use over the cell width more extreme. The increase in velocity across the width of the cell is approximately proportional to the decrease in cell thickness. But the increase is more than proportional 0.061 ms^{-1} , 0.134 ms^{-1} (prop.: 0.121 ms^{-1}) and 0.284 ms^{-1} (prop.: 0.242 ms^{-1}).

The last studied individual adjustment was the aspect ratio with the result presented in figure 4.3.d. For aspect ratios towards ∞ the velocity over the cell width becomes constant because the cell width goes to zero. This results in an ideal homogeneous flow. For low aspect ratio values the flow needs a strong steering to be homogeneously distributed over the full cell width. But low aspect ratio results in low pressure drop. Comparing the three modelled aspect ratios, an aspect ratio of 1 shows the most narrow velocity distribution, though the differences are limited ($\leq 0.003\text{ ms}^{-1}$).

Figure 4.3 showed only the velocity at a single level in the flow domain, but it is also important to include the flow behaviour at other locations. Therefore a homogeneity value is defined taking into account the velocity at several levels. The homogeneity is derived using the standard deviation of the velocity values for constant y coordinates, see equation (4.1). σ is the standard deviation, v the vertical velocity in ms^{-1} and x the location of the velocity measurement in m. The homogeneity, electrode area and pressure drop values for all modelled designs are presented in table 4.1. The pressure drop values in the table are only a rough indication, because these numbers seem to be sensitive to grid coarseness and quality.

$$\text{Homogeneity} = \frac{3}{\sigma(v(x, -0.044\text{ m}, 0\text{ m})) + \sigma(v(x, 0\text{ m}, 0\text{ m})) + \sigma(v(x, 0.044\text{ m}, 0\text{ m}))} \quad (4.1)$$

The most obvious difference among the first modelling iteration is the pressure drop when the thickness is varied, figure 4.4.a. Homogeneity increases with cell thickness and cross sectional area of the inlet and outlet pipes. Pressure drop reduces also when the size of the inlet and outlet pipes is increased, figure 4.4.c. From this first iteration can be concluded that channels, increasing the pipe diameters and adding a constriction are a suitable strategies to improve the flow distribution.

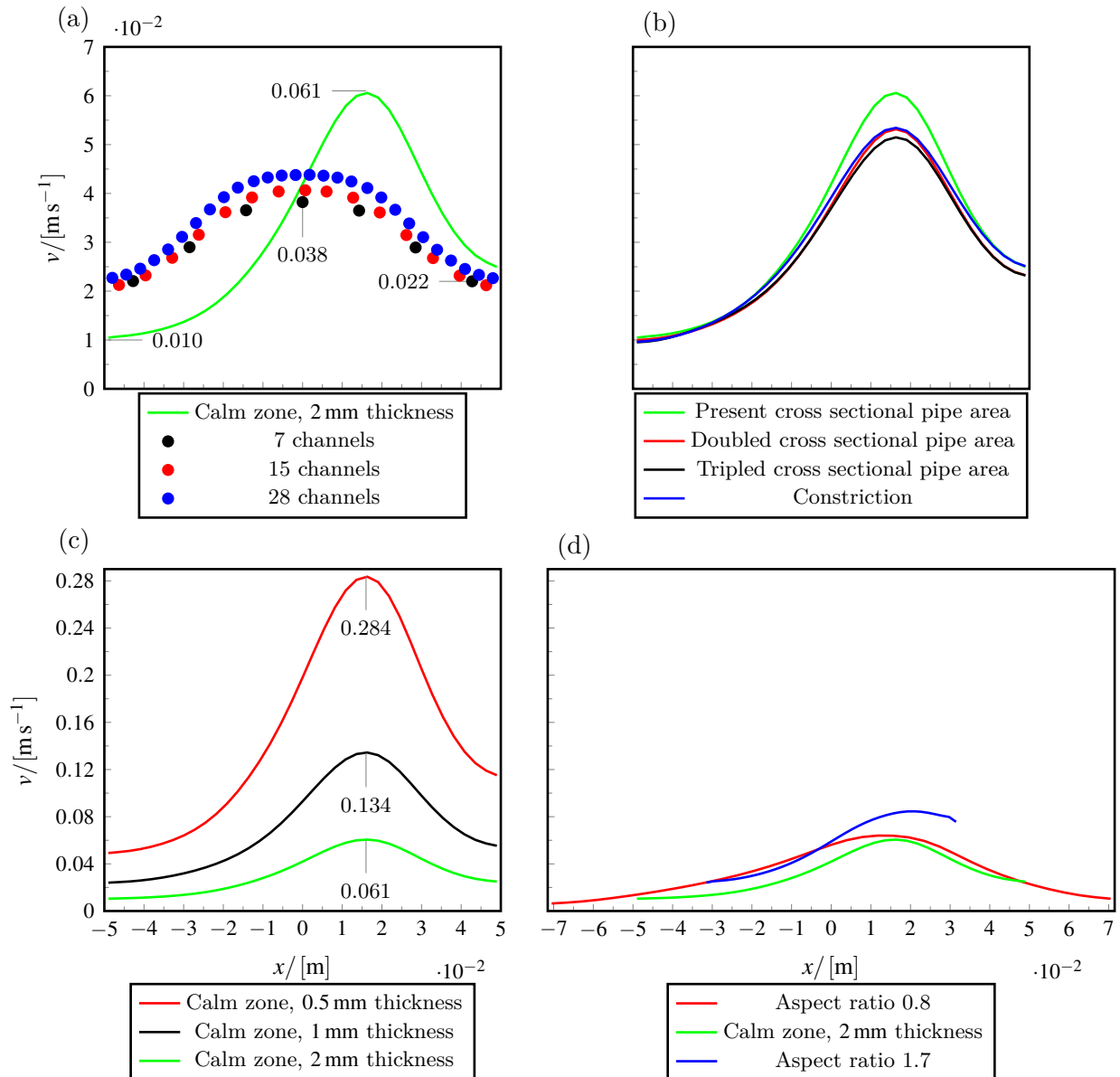


Figure 4.3: The vertical velocity at $y = -0.044\text{m}$ to compare modelled design ideas. (a) The effect of several numbers of channels, compared to the starting point design (green line). (b) The effect of the cross sectional area of the inlet and outlet pipe to and from the cell. (c) The effect of varying the cell thickness. The increase in velocity across the width of the cell is approximately proportional to the decrease in cell thickness. The actual increase in velocity is higher. (d) The effect of changing the aspect ratio.

Table 4.1: Overview of the characteristics of the design ideas considered in the first modelling round.

Design idea	Electrode area (m ²)	Homogeneity	Pressure drop (Pa)
Calm zone, thickness 0.5 mm	0.0122	37	2627
Calm zone, thickness 1 mm	0.0123	40	525
Calm zone, thickness 2 mm	0.0127	43	134
7 channels	0.0148	45	169
15 channels	0.0176	35	176
28 channels	0.0222	34	180
Doubled cross-sectional area inlet	0.0127	50	92
Tripled cross-sectional area inlet	0.0127	52	75
Constriction	0.0127	99	200
Aspect ratio of 0.8	0.0180	35	127
Aspect ratio of 1.7	0.0085	33	132

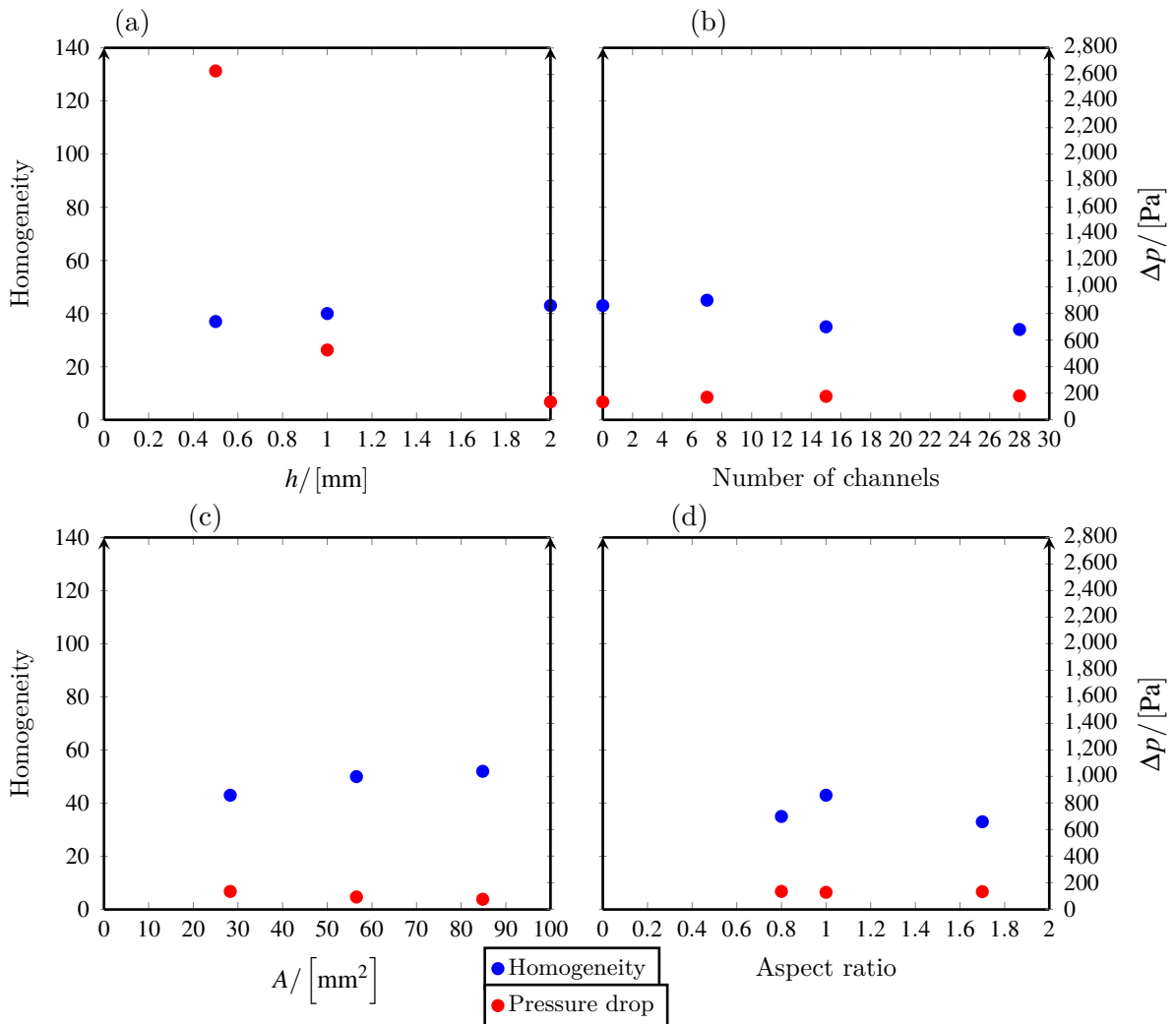


Figure 4.4: Effect of several parameters on the homogeneity and pressure drop investigated in the first modelling iteration: (a) The effect of cell thickness, (b) the effect of the number of channels, (c) the effect of the cross sectional area of the inlet and outlet pipe, and (d) the effect of the aspect ratio.

4.3. Second CFD screening

In the first modelling iteration emphasis was on individual adjustments. In this second iteration the combination of adjustments is examined. For example the constriction is combined with larger inlet and outlet pipes. Next, channels were added. Also different aspect ratios in combination with a constriction and larger pipes are analysed. The goal of this second iteration was to come to more prototype like designs, so designs with adjustments combined.

Only a single calm zone was studied in the first screening, so in the second modelling iteration also variations to this calm zone were considered, see figure 4.5. As already mentioned, the length and the number of channels can be varied. Varying the number of channels is already studied in the first modelling iteration. In this second iteration varying the channel length over the cell width is also assessed, figure 4.6.

The starting point for the thickness in this second screening round is 1 mm. This thickness was chosen for two reasons. Firstly, the first modelling round showed that it is more challenging to obtain a homogeneous flow distribution in a narrower cell. Therefore, we focus on optimizing the flow distribution even in cells with a limited thickness. Secondly, some calm zone geometries depend on the cell thickness. Limiting the cell thickness assesses these geometries in a more critical range. This applies especially to the constriction and the manifold like geometry introduced in section 5.1.

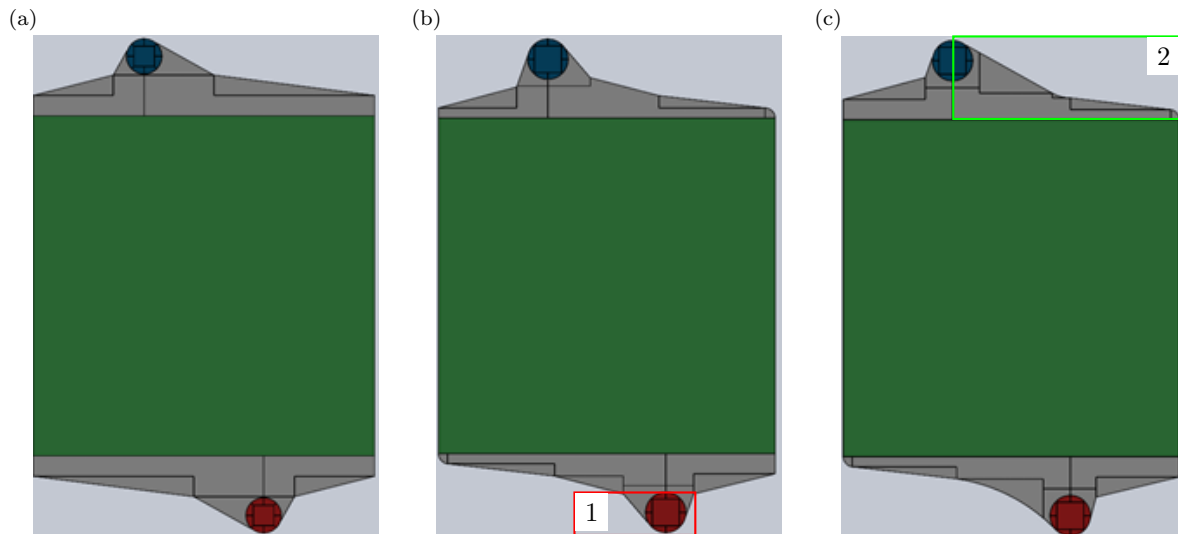


Figure 4.5: Variations to the calm zone design. (a) The calm zone design as studied in the first modelling iteration. (b) A smaller angle (60°) in the first part of the calm zone (1). (c) Modification in the top part of the calm zone (2).



Figure 4.6: A variation to the design with the channels, the channel length is varied over the cell width.

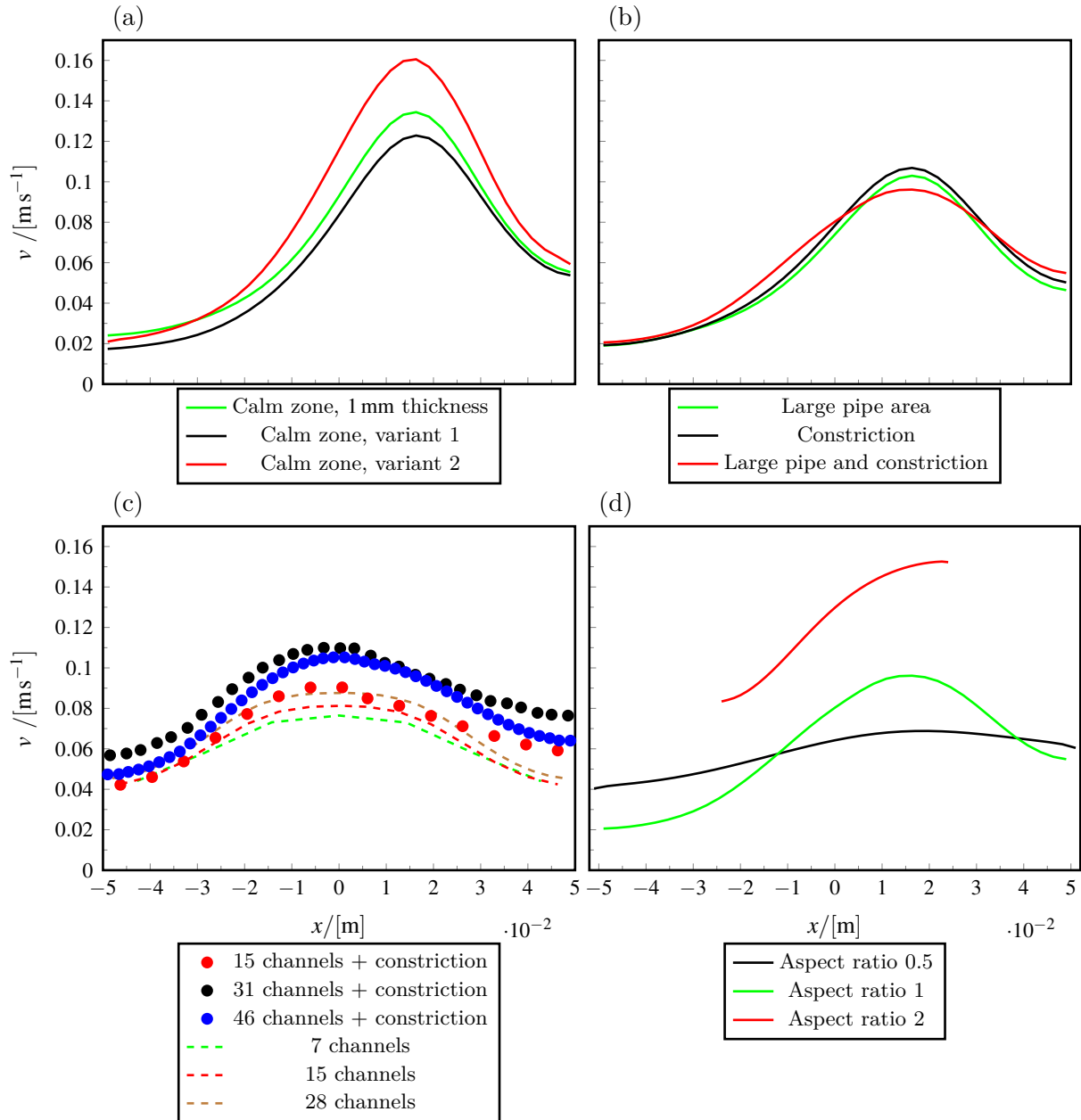


Figure 4.7: The vertical velocity at $y = -0.044\text{m}$ to compare the combination of design ideas. (a) Different calm zones and a larger cross sectional area of the inlet and outlet pipe combined. (b) The calm zone with larger inlet and outlet pipe versus a design which has a constriction too. (c) Designs with channels, larger inlet and outlet pipe and a constriction, compared to the design with channels in the first modelling round. (d) Aspect ratios of 0.5, 1 and 2 compared.

Varying the geometry of the calm zone according to figure 4.5 did not show a significant improvement, figure 4.7.a. Variant 2 scored even worse. When the constriction is combined with a larger cross sectional area of the inlet and outlet pipes, the velocity distribution is further improved, figure 4.7.b.

Combining the channels with the constriction results in a similar velocity distribution as without constriction, figure 4.7.c. It should be noted here that the cell thickness for the designs with a constriction is 1 mm and that the channels in the first iteration were modelled with a 2 mm cell thickness. From figure 4.3.c became clear that reducing the thickness is not beneficial for the homogeneity. Though the effect of the constriction is not clear when it is combined with channels, the effect of varying the channel length is visible. Especially at the right side of the cell the difference between the minimum and maximum velocity is reduced.

Figure 4.7.d shows that the combination of a low aspect ratio and the constriction significantly improves the velocity distribution. It should be noted here that the inlet and outlet are for all aspect ratios at the same location. This is beneficial for the aspect ratio of 0.5, because the length of the calm zone increases.

An overview of the results of the second modelling iteration is given in table 4.2. Again applies that the pressure drop values are only a rough indication. The cell thickness of 1 mm in the second modelling round explains the different order of magnitude of pressure drop values compared to the first modelling iteration.

From this second iteration it is obvious that the pressure drop increases with aspect ratio, figure 4.8.b. So, from a pressure drop point of view it is preferable to keep the aspect ratio low. The highest homogeneity is found for low aspect ratio. Again no clear relation found between number of channels and its influence on homogeneity or pressure drop. It is therefore recommended to take the electrochemical aspects into account when looking for the optimal number of channels.

Table 4.2: The characteristics of the designs considered in the second modelling iteration.

Design idea	Electrode area (m ²)	Homogeneity	Pressure drop (Pa)
Calm zone variant 1	0.0115	43	352
Calm zone variant 2	0.0117	33	237
Constriction	0.0109	50	1134
15 channels	0.0133	54	1100
31 channels	0.0156	41	1019
46 channels	0.0179	41	1365
Aspect ratio of 0.5	0.0054	122	994
Aspect ratio of 2	0.0050	75	2077

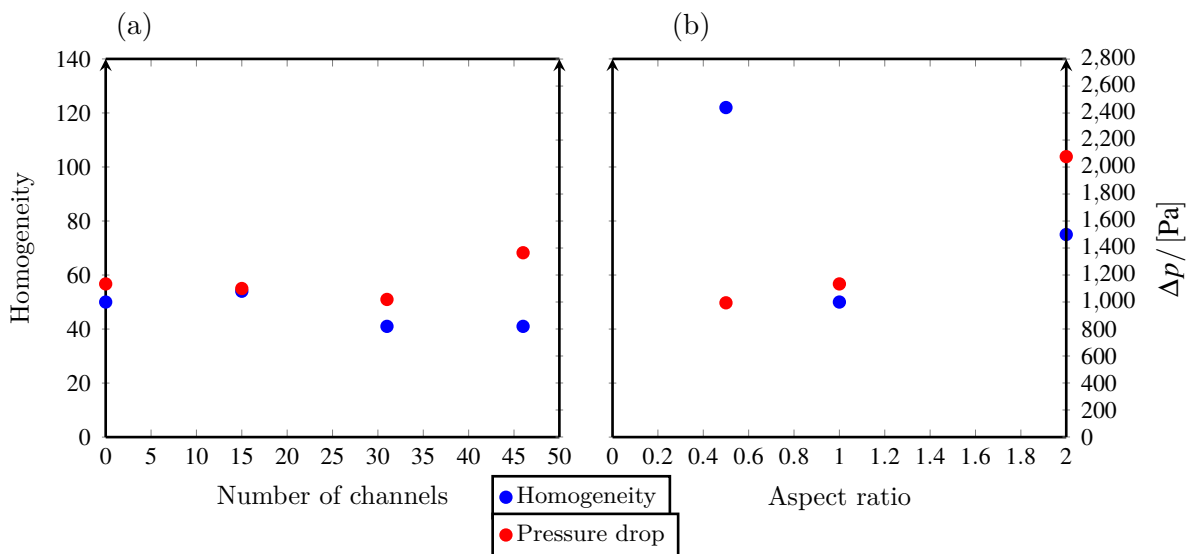


Figure 4.8: Effect of several parameters on the homogeneity and pressure drop investigated in the second modelling iteration: (a) the effect of the number of channels, and (b) the effect of the aspect ratio.

4.4. Conclusion and final selection of designs

From the numerical work can be concluded that a larger cross sectional area of the inlet and outlet pipes is preferred. A geometry to distribute the flow evenly over the cell width, like a constriction, shows promising results. Channels increase both the electrode area and the homogeneity of the flow.

Two designs which were too complex to model, are experimentally assessed in the next chapter. Also a number of adjustments assessed in this part are experimentally examined to check whether the numerical screening points in the same direction as the experimental results.

5. Experimental results and discussion

After a numerical investigation in chapter 4, this chapter discusses the experimental investigation. This experimental research focusses on the present cell, the calm zone design, cell thickness, channels and cross sectional area of the inlet and outlet pipes. These cell configurations were selected for experiments to check whether the CFD screening shows the same trends. Note that the experimental work was not used to validate the model, but rather, to check whether the experimental data show similar trend as the CFD results. Two other designs, namely a net in the interelectrode gap and a manifold geometry in the calm zone, were also evaluated. These design were not modelled because of their complexity.

The focus in this chapter is successively on the flow distribution, bubble behaviour and the behaviour in the high pressure reactor. Bubbles were neglected in the CFD model, but are included in the experiments to be able to assess the designs in this area too.

5.1. Flow distribution

The flow distribution in the conventional design is highly dependent on the inflow. Downstream of the inlet a jet is visible, the dark blue area in figure 5.1a. The flow distribution is visualized using the arrival time of ink. The liquid entered the visualization cell at the bottom and left at the top. The contour plots indicate how long it takes for the ink to reach a location in the cell measured from the cell inlet.

Like for the numerical result, also here a homogeneity value is defined, to represent the fluid distribution over the full cell in a single value. The homogeneity is defined in the same way as in equation (4.1), but now all y values are taken into account. The homogeneity for the conventional design without an net is 0.3. An overview of the homogeneity values is presented in figure 5.8.

Adding a net in the inter electrode gap improves the cell use a lot for the present design, see figure 5.1b. Though the use of the top corners can still be improved. The flow is no longer concentrated on the main path from inlet to outlet, as without a net, and almost the full cell is reached within 10 s. Homogeneity: 0.4

A design with a calm zone and no channels performs similar to a design with also channels, figure 5.2. The calm zone promotes distribution of the fluid over the full cell width, figure 5.2a. Though the use of the right top corner is still limited, homogeneity: 0.7. The design with channels performs a bit worse when it comes to distributing the fluid homogeneously over the cell width, see figure 5.2b. The boundary layers at the channel walls causes higher variation in ink arrival time over the cell width, homogeneity: 0.6.

The performance of a net is similar regardless interelectrode gap size, see figure 5.3. For a 0.5 mm gap the homogeneity is 0.8 and for a 2 mm gap the homogeneity is 0.9. Noteworthy is that findings of the literature review in section 1.2.1 regarding turbulence promoters are confirmed. Figure 5.3a shows that the net touches the transparent plates in the experimental setup, the little white dots. In the electrolyser this means that the net would touch the electrode and membrane, and as a result the effective surface of the electrode and membrane is reduced. Another effect is the formation of preferential channels, which can be seen in figure 5.3b. This leads to inhomogeneity in the horizontal direction. From those results can be concluded that the inter electrode gap and the net thickness should be tuned to avoid these effects. For example, the net should always be 0.1 mm thinner than the gap but no more than 0.5 mm.

The gains of the constriction design were limited according to the numerical results in the previous chapter. Therefore an alternative is introduced which, because of its complexity, is only experimentally investigated. Figure 5.4 shows this alternative. This manifold like geometry in

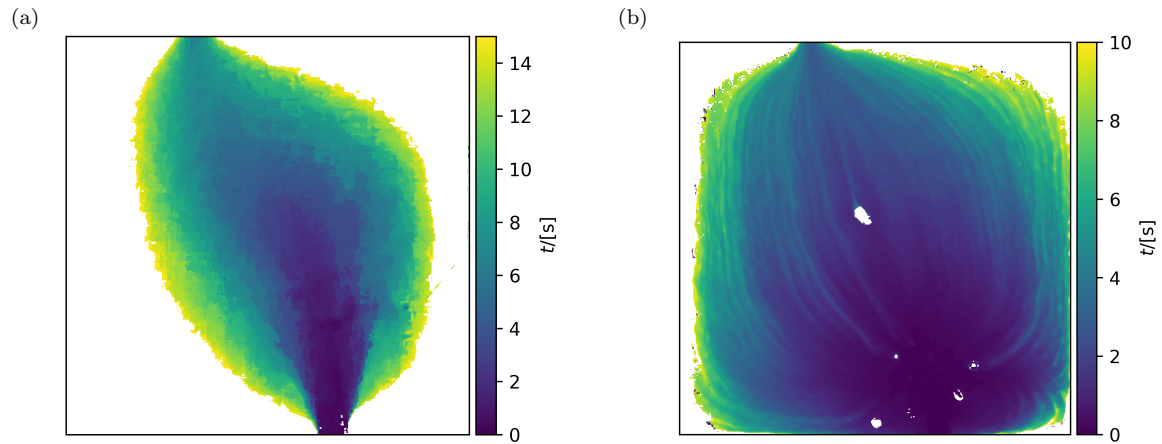


Figure 5.1: Contours of the ink arrival time measured from the cell inlet at the bottom. (a) Conventional design, as shown in figure 4.1a. It takes ~ 7 s for the ink to reach the outlet and it takes much longer than 15 s to reach the whole cell. The white indicates the area that is not reached within 15 s. Homogeneity: 0.3. (b) Conventional design with net, almost the full cell is reached within 10 s. Homogeneity: 0.4.

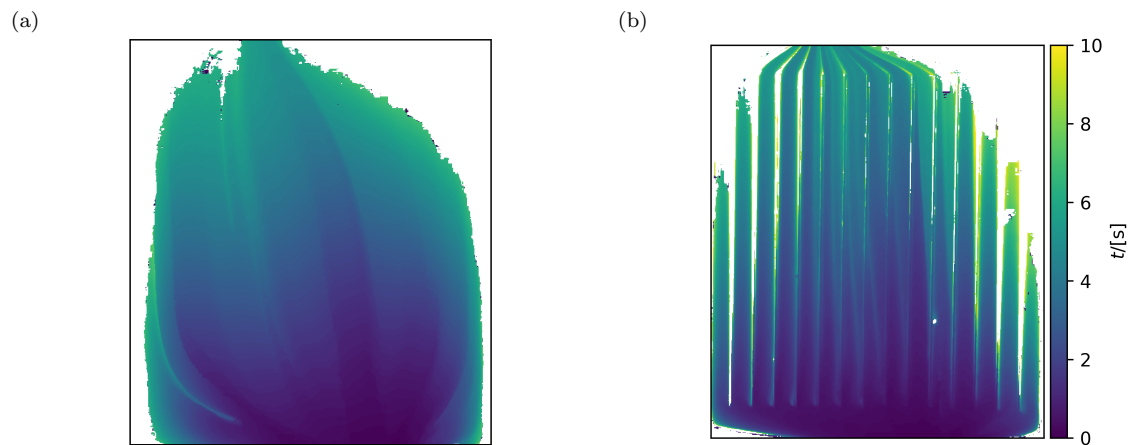


Figure 5.2: The effect of channels, contours of ink arrival time for the calm zone design and a design with channels. (a) Calm zone with 2 mm cell thickness, homogeneity: 0.7. (b) Design with a calm zone and 15 channels, homogeneity: 0.6.

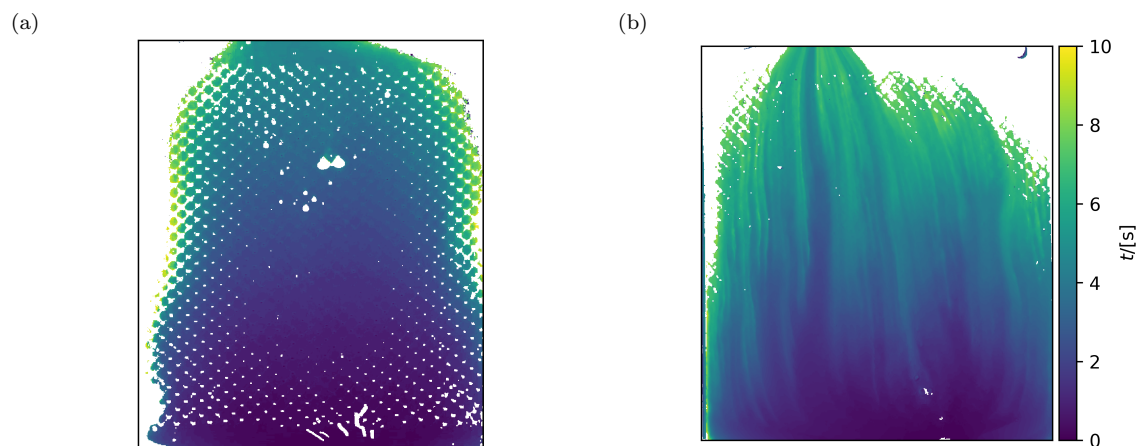


Figure 5.3: The effect of cell thickness with a net, contours of ink arrival time for the calm zone design with a net. (a) 0.5 mm cell thickness. The white dots indicate that the net is touching the cell walls. Homogeneity: 0.8. (b) 2 mm cell thickness. The fluid follows preferential channels. Homogeneity: 0.9.

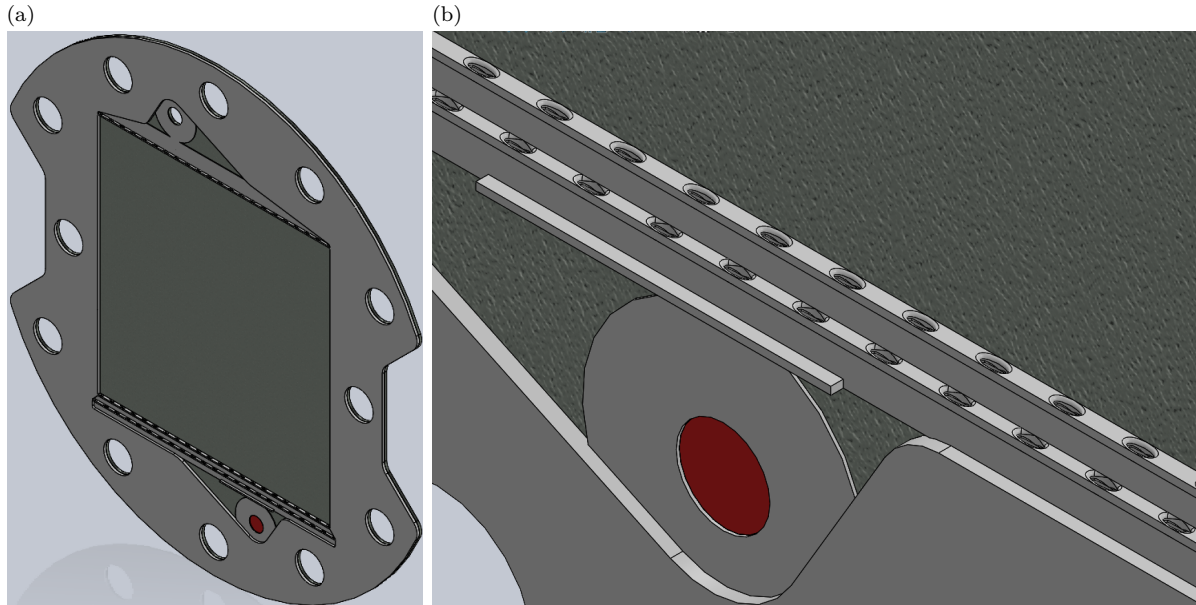


Figure 5.4: A manifold like geometry in the calm zone to distribute the flow equally over the cell width. (a) The dark grey indicates the electrode and the electrolyte flows upwards in the channel created by the light grey spacer. The outer diameter is 0.19 m. (b) The red circle indicates where the electrolyte enters the 1 mm interelectrode gap. A baffle is placed right above this inlet. The manifold consists of two beams with oval holes.

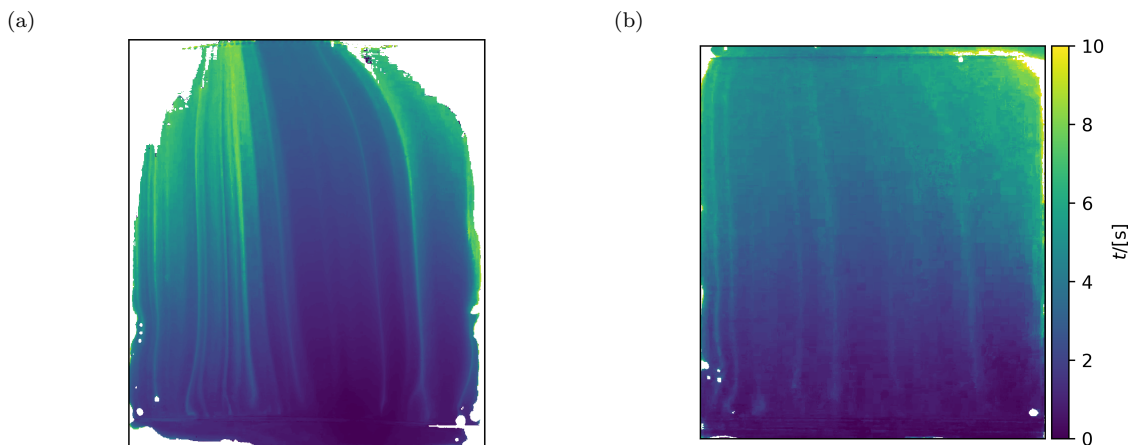


Figure 5.5: The effect of an advanced calm zone, contours of ink arrival time. (a) For a design with a constriction in the calm zone, homogeneity: 0.8. (b) For a design with a manifold like geometry in the calm zone, homogeneity: 1.4.

the calm zone performs the best of all experimentally investigated designs, figure 5.5b. The ink arrival time is almost constant over the cell width, homogeneity: 1.4. The constriction, figure 5.5a, shows that almost the full cell is reached but large variation of ink arrival time over the cell width, homogeneity: 0.8.

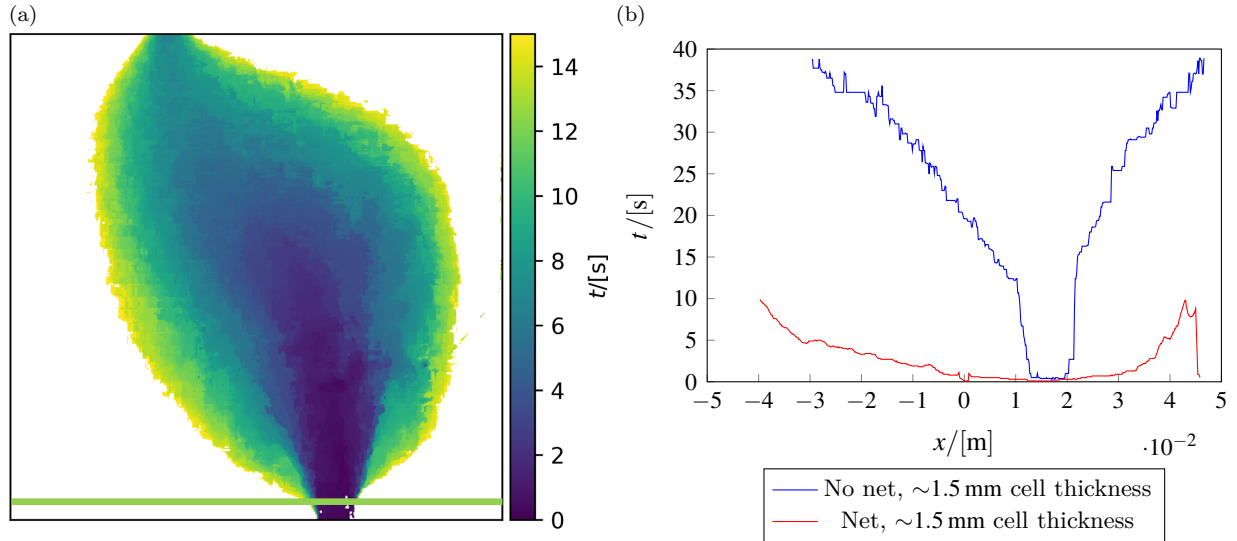


Figure 5.6: Ink arrival time at $y = -0.044$ m. (a) The green line is the location where the ink arrival time is measured. (b) The ink arrival time over the cell width plotted for the two present configurations. The blue graph does not cover the full width of the cell, because the recording was stopped before the ink arrived over the full cell width.

The contour plots with ink arrival times contain a lot of data which makes it hard to compare several design ideas at a glance. Therefore graphs are derived of the ink arrival time at $y = -0.044$ m for all experimentally investigated designs. In figure 5.6a this location is indicated. Figure 5.6b shows for the present design without and with a net the graph of the ink arrival time. In figure 5.7 all the experimental results of the ink arrival time are put together.

Figure 5.7 shows that the present design without net has a highly uneven ink arrival time compared to all the other configurations. The second worst is the present design with a net. All other designs perform better. Note that the channel walls are clearly visible in the magenta graph.

One difference between the present design and all the others is the calm zone. So, it can be concluded that a calm zone has a positive impact on flow distribution. The design which performs clearly the best for ink arrival time is the design with the manifold like geometry. Both figure 5.5b and 5.7.c show for this design that the cell is evenly used.

From the ink experiments can be concluded that the design with the manifold performs the best. Another promising design is the design with a calm zone and a net, but the net thickness should be tuned to the cell width.

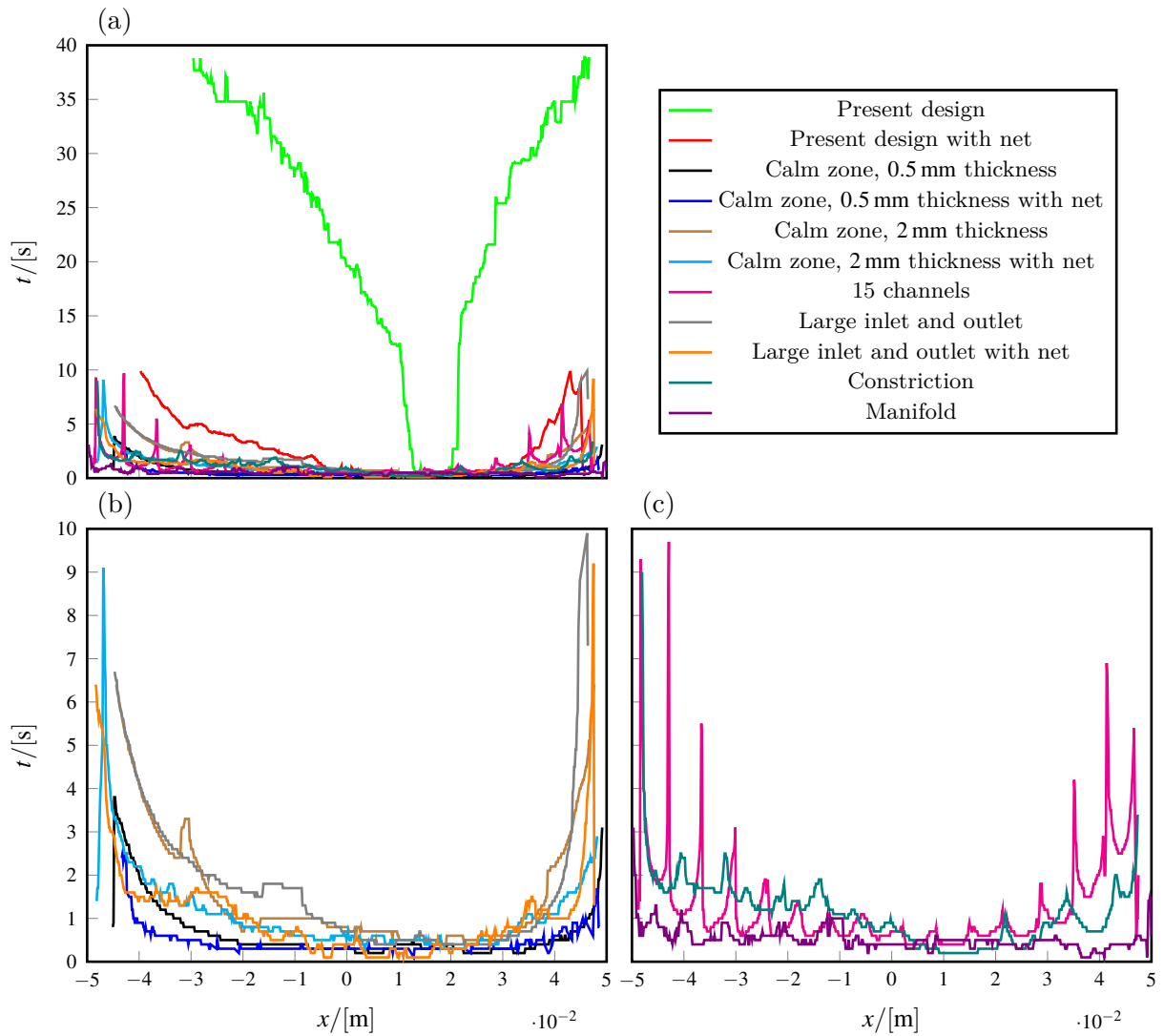


Figure 5.7: Ink arrival time at $y = -0.044\text{m}$ for all the experimentally assessed design ideas. This is the extended version of figure 5.6b. (a) Shows an overview of all tested designs. (b) Focuses on the effect of calm zone, interelectrode gap and larger pipes. (c) Presents the effect of a geometry in the calm zone or interelectrode gap.

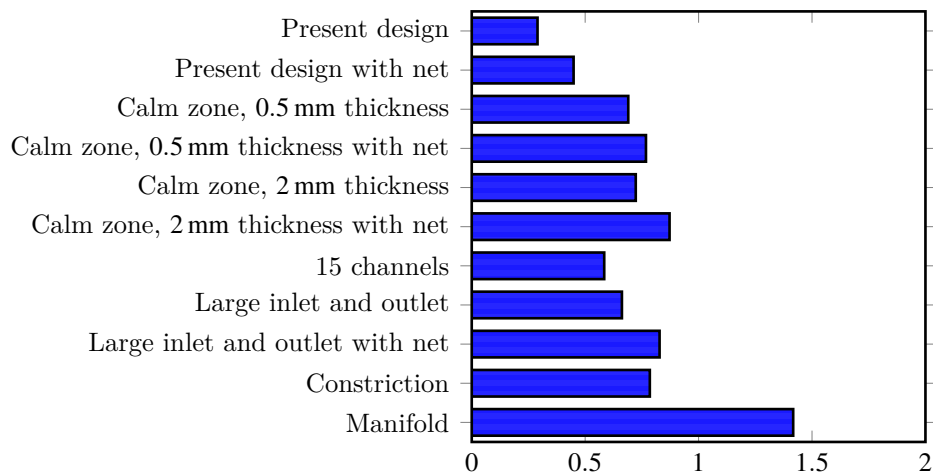


Figure 5.8: Graphical representation of the homogeneity values for all the experimentally assessed design ideas. The homogeneity is defined in the same way as in equation (4.1), but now all y values are taken into account.

5.2. Bubble behaviour

This section focusses on bubble behaviour that has been ignored until now. A clear difference is seen in the gas behaviour depending on the application of a net for the conventional design. Without a net the cell state goes through the cycle as presented in figure 5.9. First, bubbles enter and rise to the top where gas accumulates. Second, this accumulated gas pocket grows to a critical size. And finally, the accumulated gas pocket reaches a critical size and escapes, whereafter this cycle repeats. Bubbles are routed by the net, when a net is added, see figure 5.10. Bubbles tend to get stuck in the net rather than the gas accumulating at the top. This results in a higher, and more stable, gas fraction.

The designs with an inter electrode gap of 0.5 mm thickness have a high gas fraction compared to the 2 mm cells, figure 5.11. This is a result of the bubbles being squeezed between the cell walls, which made bubble movement through the cell difficult.

The gas fraction in the present design is clearly periodic (green line in figure 5.11) in agreement with cycle previously described, see figure 5.9. The other designs have the calm zone which allows for easier bubble removal, figure 4.1, preventing bubble accumulation.

At this point can be concluded that the gas fraction is low when the top part of the cell geometry slopes towards the outlet. Channels do not influence the gas fraction. In these experimental results a narrow cell has a high gas fraction, but the bubble size in the experiments was larger (0.8 to 2 mm) than the expected size in the reactor, see section 1.3.4. Also smaller bubbles are less likely to get stuck in the net. Therefore it cannot be stated that a narrow cell will have a high gas fraction based on this experimental results.

Combining the results of section 5.1 and this section, the calm zone design with 2 mm thickness, the channels and the manifold design are the most promising, see figures 5.8 and 5.11. The manifold had the highest score in the previous section and also the gas fraction is limited. The channels and the 2 mm calm zone have a slightly lower gas fraction, but a clearly lower score on homogeneous fluid distribution.

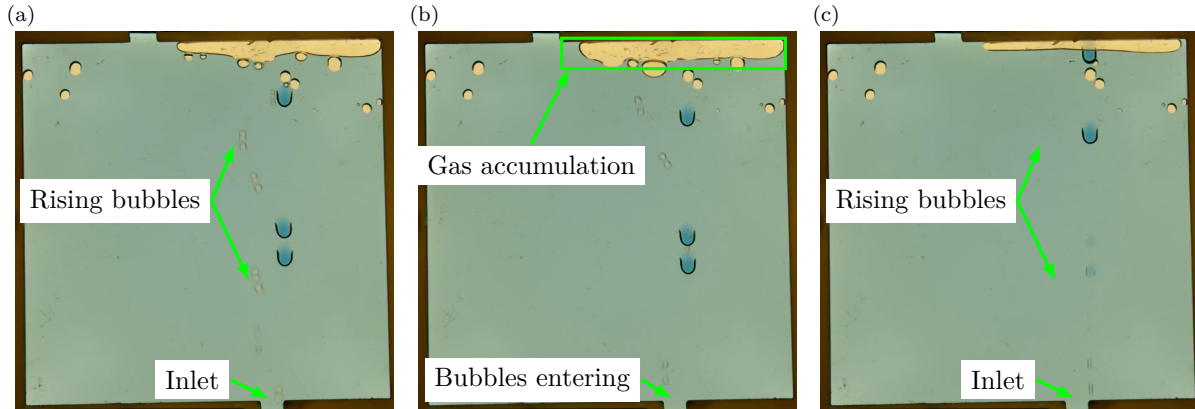


Figure 5.9: The repeating cycle of bubbles in the experimental visualisation cell without a net. (a) Bubbles entering the cell from the inlet at the bottom and rising to the top, $t = 9$ s. (b) Gas accumulation at the top of the cell till the accumulated bubble reaches a critical size, $t = 13$ s. (c) The accumulated bubble is escaped from the cell and this cycle repeats itself, $t = 16$ s.

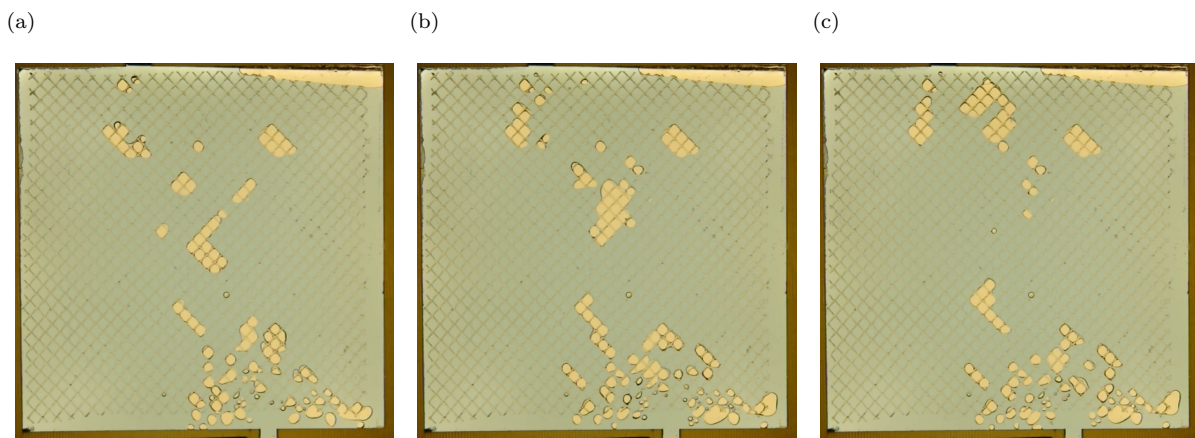


Figure 5.10: The experimental bubble behaviour with a net, the bubbles are routed by the net. (a) $t = 0$ s, (b) $t = 50$ s and (c) $t = 60$ s, the gas fraction shows only minor variations.

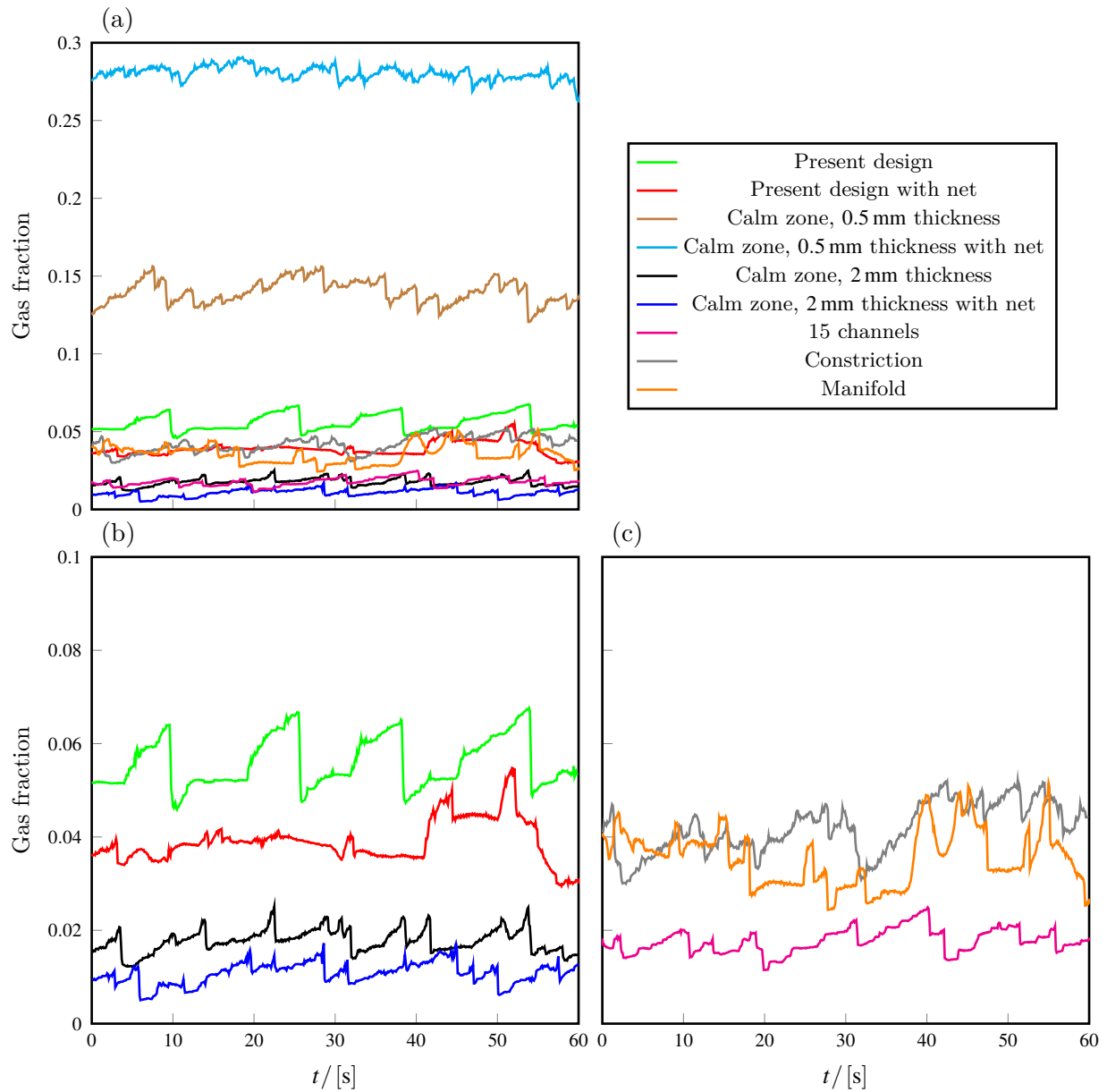


Figure 5.11: Gas fraction in the cell for the experimentally assessed design ideas over a period of 60 s (a). Detail view of: (b) the designs without and with a calm zone with 2 mm thickness, and (c) the designs with channels and a geometry in the calm zone.

5.3. Bubble visualization in the high pressure reactor

The results discussed in the first and second section of this chapter were obtained in a visualization cell at atmospheric pressure with no current applied. This allowed for visual assessment of flow and bubble behaviour, but the conditions are not fully representative for the lab scale reactor. Understanding the type and amount of bubbles in realistic condition is essential for optimizing the flow channels between the electrodes. In the lab scale reactor the effect of current, pressure and flow rate on nucleation and bubble size were studied for the present design.

Before presenting the results with the high pressure electrolyser, one should be aware of the differences with the experimental setup. First the liquid, in the experiments demineralized water was used, in the electrolyser a KOH solution (1 mol kg^{-1}). Second the gas, in the experiments air, in the electrolyser $\text{CO}_2, \text{H}_2, \text{O}_2$. Thirdly the pressure, in the experimental setup atmospheric, and in the electrolyser variable up to 40 bar. Fourthly bubble generation, in the experimental setup bubbles were injected in the inflow to the cell, in the electrolyser bubbles are formed as a result of nucleation. Finally the bubble size, in the experimental setup 0.8 to 2 mm, and in the electrolyser 5 to $20 \times 10^{-2} \text{ mm}$.

Despite this differences, the experimental setup still allowed to study bubble movement, coalescence and breakup, with limited requirements for the camera. Observing smaller bubbles in the full cell would request a sophisticated camera. Different rising velocities of bubbles were observed based on bubble size and it was noted that small bubbles are entrained with the flow in agreement with the findings in section 1.3.4. The larger bubble size in the experimental setup basically means that the designs are tested in more extreme conditions. Big bubbles get easier stuck than small ones.

A consequence of the smaller bubbles in the actual reactor is that the cycle lead time (figure 5.9) increases, as a result of less big bubbles to feed the gas pocket. Because of this we hypothesise that the differences without and with a net are less pronounced in the actual reactor. The accumulated bubble is expected to grow slower and the bubbles are less likely to get stuck in the net, resulting in a lower gas fraction than in the experimental setup.

When running the high pressure reactor without current, no nucleation was observed. So there is no nucleation as a result of pressure drop over the cell due to pumping liquid through the cell. Gas nucleation occurs as soon as current is applied, even from small values, like 0.2 A. The observed bubbles can be divided into three types, (i) big bubbles with a radius of $\sim 5 \text{ mm}$, (ii) small bubbles with a radius of $\sim 0.5 \text{ mm}$ and (iii) smoke. The smoke makes that the solution looks foggy. See figure 5.12 for pictures of the bubble types.

The development of the big bubbles remains unclear, because the information about what happens between the cell and the sight glass is limited. It is possible that the big bubble gets its final size within the cell. Another possibility is that the big bubble obtains its final size in the line between the cell and the sight glass. An explanation for this could be that in the line coalescence occurs, forming larger bubbles. Considering the electrolyte discharge lines (figure 5.13), bubble coalescence is very likely because of all the bends and the slope changes. Formation of big bubbles was not observed in the experimental setup when a net was applied and in the high pressure electrolyser it was. Therefore we hypothesise that big bubbles are formed when the gas has left the interelectrode gap.

The experimental findings with the high pressure reactor for the present design including a hypothesis are presented in table 5.1.

It is likely that the gas at the cathode side mostly contained H_2 and possibly some nucleated CO_2 . We confirmed the presence of H_2 by running the high pressure reactor without CO_2 , which did not result into a noticeable change in bubble types and amount. Unfortunately, we could not confirm the presence of CO_2 gas. We believe that adding a gas chromatograph to the high pressure setup as well as designing new experiments could answer this question in future studies.

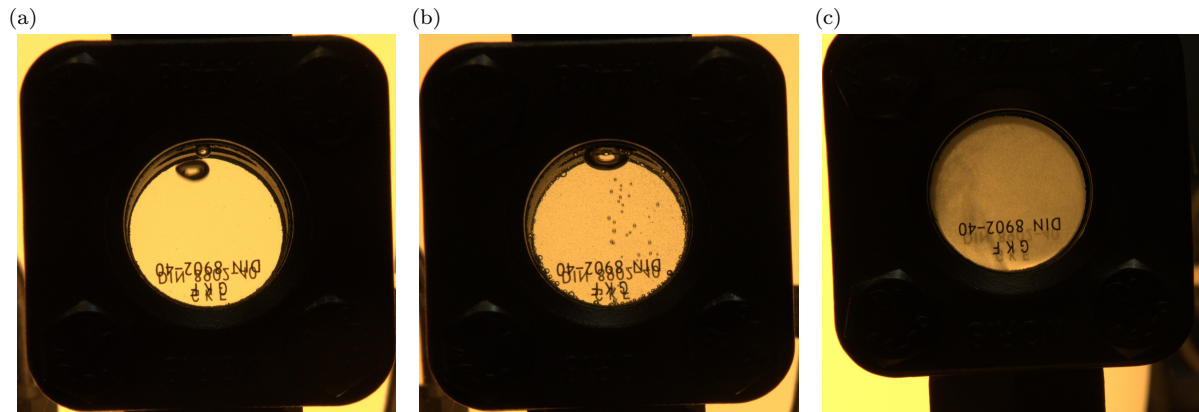


Figure 5.12: Different types of bubbles seen through a 32 mm diameter sight glass in the reactor outflow line of the high pressure electrolyser setup. For the experimental setup and the location of the sight glass see figures 3.1 and 5.13. (a) A big bubble, (b) small bubbles, and (c) smoke.

Table 5.1: Overview of the findings when performing the experiments in table 3.1. A hypothesis is given for each observation.

Finding	Hypothesis
Higher current density \rightarrow higher gas fraction.	The reaction rate is increased because the electron transport is accelerated, so also more gaseous product is formed.
Bubble size is independent on current density.	For this setup the current density has a limited effect on bubble size. So, bubble nucleation might be dominant over bubble growth.
Lower pressure 0 to 20 bar \rightarrow larger bubbles.	Gas occupies a larger space under lower pressure, when the amount and temperature of the gas are kept constant.
Higher pressure \sim 40 bar \rightarrow more smoke.	The bubble size is reduced as the pressure is increased. Gas occupies a smaller space under higher pressure, when the amount and temperature of the gas are kept constant.
Higher pressure \sim 40 bar \rightarrow less bubbles.	The solubility of gases increases with pressure, so the driving force for nucleation is lower. Less H_2 might be produced as more CO_2 is available for the reaction. Which is a result of increasing CO_2 solubility with pressure.
Higher flow rate \rightarrow more smoke.	The amount of dissolved gas is kept low by the high inflow of new reactants, and therefore the amount of dissolved gas available for bubble growth is limited. As a result, the bubbles remain small.
Higher flow rate \rightarrow higher gas fraction in catholyte.	This phenomenon is to be investigated further for better understanding of the reactor.
Higher flow rate \rightarrow smaller bubbles.	The amount of dissolved gas is kept low by the high inflow of new reactants, and therefore the amount of dissolved gas available for bubble growth is limited. As a result, the bubbles remain small.
Nucleation is not stopped by increasing the flow rate.	The amount of dissolved gas cannot easily be lowered to a value below the threshold for nucleation by increasing flow rate.

This experiment with the high pressure reactor has shown that bubbles are always present during the electrochemical reaction. This emphasizes the importance of gas bubble mitigation.

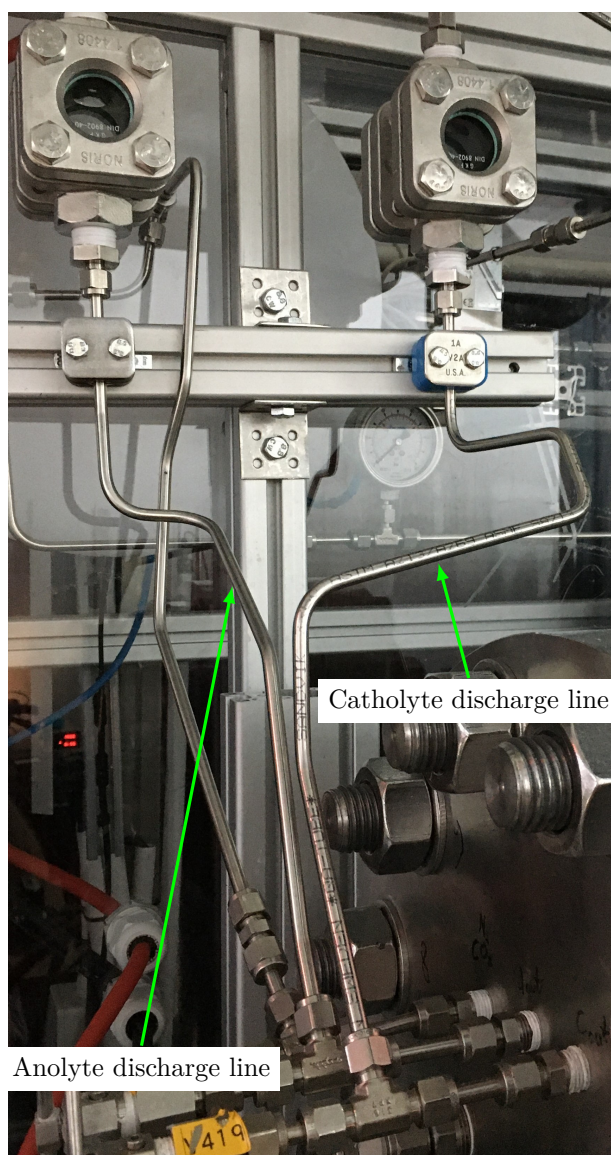


Figure 5.13: Part of the higher pressure electrolyser setup showing the anolyte and catholyte discharge lines from the reactor to the sight glass. The outer diameter of the lines is 6.35 mm.

5.4. Prototyping

The next step after assessing designs in the experimental setup and studying the present design in the high pressure reactor, is to manufacture prototypes to be tested in the high pressure reactor. Two prototypes were manufactured, one with a manifold and one with channels. The manifold design was chosen because it scored well in the experimental setup. The design with channels was chosen because it showed promising results in the CFD screening. Another reason to select the channel design for a prototype is that its gains are partially expected on the electrochemical level, because of the locally reduced interelectrode gap as a result of the electrode geometry. The manifold design is manufactured using 3D printing of Polylactic acid (PLA). Because of its complexity it cannot be cut out of sheet material like the present spacer which defines the interelectrode gap in the high pressure setup. A drawing of this prototype can be found in appendix A.

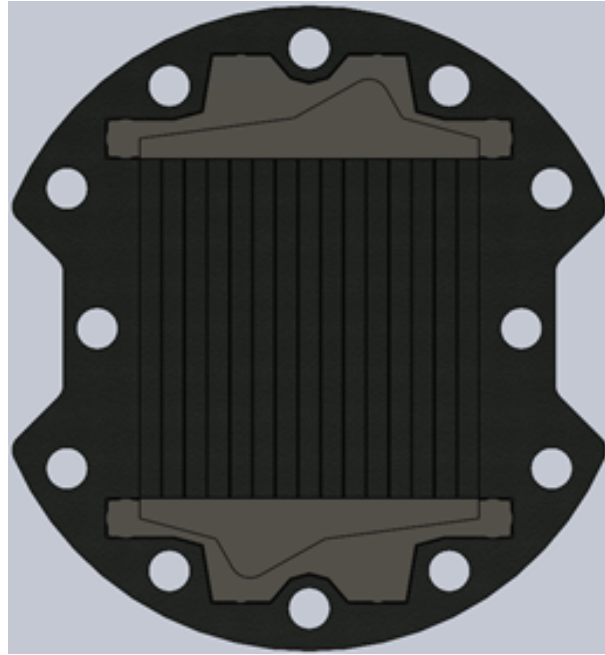


Figure 5.14: A front view of the design with channels which is an assembly of a tin plate (dark grey) and two 3D printed PLA inserts. The electrolyte enters perpendicular to the cell in the bottom light coloured part where it is spread across the 15 channels. Then the electrolyte flows vertically to the top through the channels. In the top light coloured part all the electrolyte is gathered and leaves perpendicular to the cell. The 12 holes are used to mount the electrode in the stack. The outer diameter is 190 mm, the total width of the electrolyte flow channel is 100 mm and the a single channel has a width of 6.2 mm.

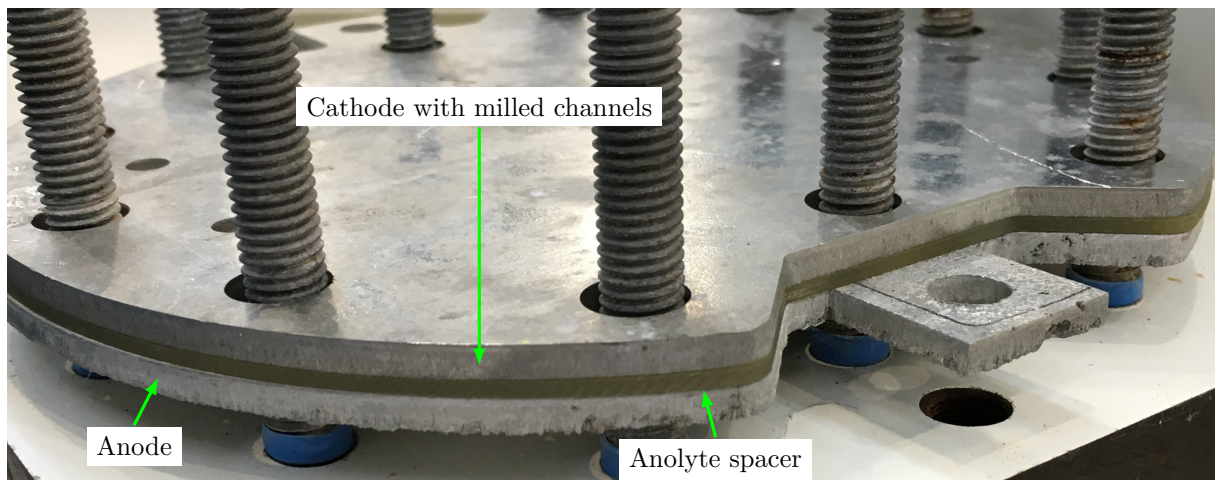


Figure 5.15: The stack with the channel design mounted. The outer diameter of the parts is 190 mm and the thickness of the cathode and anode is 5 mm. The membrane which separates the anolyte and the catholyte is located between the anolyte spacer and the cathode.

The design with channels is produced with a combination of techniques. Figure 5.14 shows the front view of the 3D model of the assembly of this design, more details can be found in appendix A. The production of the tin plate was performed in three steps: (i) casting, (ii) cutting and (iii) milling. A tin block was melted and cast to form a 5 mm thick plate. Laser cutting was used to cut the plate to the right size and to create the holes to fix the plate in the setup. Finally, the channels and the cavities were created using milling. These cavities were created to have the flexibility to adjust the calm zone. 3D printed inserts were put inside the cavities which are easily replaced by other inserts. Figure 5.15 shows a picture of the mounted stack.



Figure 5.16: The result of chemical and mechanical loading on the insert and spacer. (a) Lamination of the insert, probably as a result of the acidic or alkaline environment. The channel width of this design is 6.2 mm. (b) Deformation of the insert because the fit in the cavity was too tight. (c) A crack in the spacer as a result of mechanical loading.

Unfortunately, we did not succeed to test the prototypes in the high pressure reactor due to unforeseen challenges:

- Without gaskets it turned out to be difficult to avoid leakage. Liquid leaked out of the interelectrode gap and the supply lines. This is possibly due to the rough surface finish of the 3D printed parts.
- In addition to leakage to the outside, there was also internal leakage between the anolyte and catholyte side.
- The PLA material was too weak to resist the mechanical stress as a result of tightening the bolts of the stack. One of the cracks is visible in figure 5.16c.
- The fit of the inserts was too tight. Also the cavity was not deep enough, making the inserts protrude above the surface of the tin plate. The latter was a reason for high mechanical load on the insert when mounting the stack. Figure 5.16b shows the consequence of the protruding insert and the fit being too tight, resulting in a curvature.
- PLA was found not to be suitable for acidic and alkaline environments, like in the high pressure reactor. The PLA laminated possibly as a result of the chemical load, figure 5.16a. PLA is not durable in environments with $pH < 4$ and $pH > 10$, [57].

Based on the issues encountered during this test, recommendations can be made regarding geometry and material selection:

- The spacer thickness of the anolyte spacer should be adjusted to allow for the placement of gaskets to make the stack leak tight.
- Mill a groove in the tin plate to allow for the placement of a gasket.
- Reduce the thickness of the inserts, to limit the mechanical load and to provide space for a gasket on top of the insert.
- Select a material for the insert and spacer which is: (i) suitable for acidic and alkaline environments, and (ii) strong enough to resist the mechanical stress. ABS could be a suitable alternative for a prototype. ABS is durable in strong alkalis and can be suitable for short term applications in strong acids, [57]

The selected designs for a prototype are to be tested in the high pressure electrolyser. A next step after assessing the channels and the manifold design could be to combine both adjustments. This possibly improves the fluid distribution over the channels, as figure 5.2b shows that this distribution is not optimal yet. No experimental pressure drop data was generated. So to better assess new designs, it is recommended to perform pressure drop measurements.

6. Conclusions and recommendations

As stated in chapter 1, the world's energy demand, which is mainly met by fossil sources, is rising increasing CO₂ emissions inducing climate change. In this study we investigated carbon utilization and more specifically the electrochemical reduction of CO₂ to formic acid. The main question of this thesis was: How can the current knowledge of electrolyzers be applied to improve the Coval electrolyzer design regarding flow distribution and mitigation of the impact of dissolved gas production?

The electrolyzer cell geometry adjustments considered in this study were: (i) cell thickness, (ii) channels, (iii) aspect ratio, (iv) a net, (v) a calm zone, (vi) a constriction, and (vii) a manifold. Figure 6.1 graphically presents the experimental homogeneity and gas removal values of tested designs. Cell thickness and aspect ratio are adjustments influencing the relation between flow rate and flow velocity. The CFD results showed that reducing cell thickness reduces homogeneity of the flow distribution over the cell width. Reducing the cell thickness is desirable to reduce resistance for electrical current and ion supply. A smaller interelectrode gap should not result in bubbles getting stuck.

Channels clearly improve homogeneity of the flow distribution. The channels were numerically investigated and 7, 15, 28, 31 and 46 channels were considered. The results showed that the velocity variation over the cell width is reduced by 69% when channels are applied (section 4.4). No conclusion could be drawn about the optimal number of channels based on the fluid simulations alone. So this is a possible field for further research.

A net improves the homogeneity by 19% on average, but it is important to tune the net thickness and interelectrode gap. The experiment showed namely that the net can also have negative effects, in agreement with the literature. The observed negative effects were partial blocking of the electrode and membrane surface, and the creation of preferential paths. The calm zone improves the use of the bottom cell corners, thanks to the full width inlet. This effect of the calm zone was observed both in the numerical and experimental results.

The constriction stimulates the flow to enter over the full width. And finally the manifold, it performs significantly the best of all the investigated adjustments to realise a plug flow through the entire cell. The velocity over the cell width was almost constant over the entire cell. The gas fraction is also limited for this design (sections 5.1 and 5.2).

Larger inlet and outlet pipes to and from the cell improve the homogeneity inside the cell and reduce the pressure drop in these pipes. The last makes the design more suited for stacking (section 4.4). The gas fraction in the cell remains limited as long as the top part is sloped towards the outlet, allowing for easy bubble removal (section 5.2).

The designs which show the most promising results are the channel design and the design with the manifold. Prototypes were made for those designs, but no experiments were performed in the high pressure reactor. We recommend to assess the performance of these designs in the high pressure reactor. The improvement of the channels design is partially expected on the electrochemical level because the inter electrode gap is locally reduced. Testing in the high pressure reactor will provide data to compare with the performance of the conventional design.

The channel design shows in the numerical assessment a clear improvement in fluid distribution over the cell width, but there may be potential to improve this. It is recommended to investigate whether the fluid distribution over the channels can be further improved by combining the channels with a manifold.

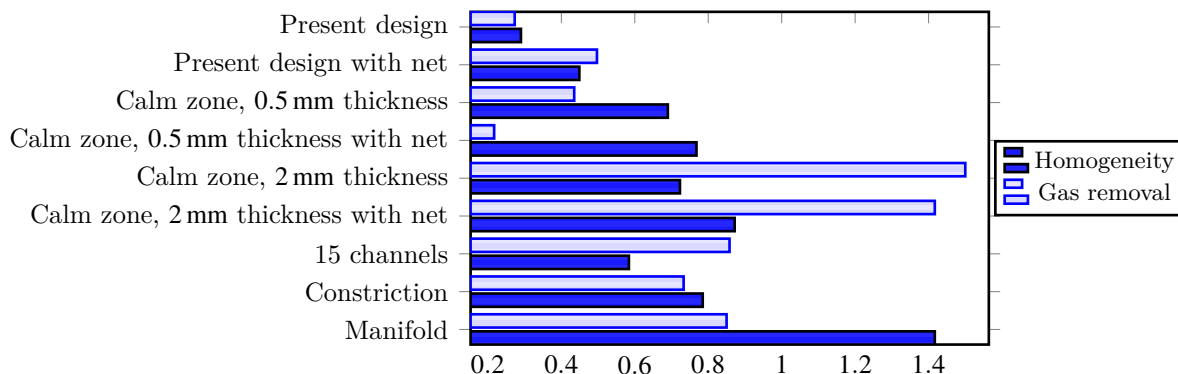


Figure 6.1: Graphical representation of the experimental homogeneity and gas removal values for the experimentally assessed design ideas. The homogeneity is defined in the same way as in equation (4.1), but now all y values are taken into account.

The prototype of the channel design was tested in the high pressure reactor. Unfortunately it was not leak tight. The leak tightness of the stack should therefore be improved, for example by implementing gaskets.

Pressure drop measurements were not performed during the experiments. Pressure drop data was thus not considered in the evaluation of the designs. It is recommended in future experiments to measure pressure drop, to better assess a design.

In the literature the electrode surface properties and the interelectrode distance were stated as areas for improvement, which were not investigated in this work. It is recommended to study also what the effects are of the electrode surface and the interelectrode distance on the electrolyser performance and whether this is a potential area for improvement.

A higher KOH concentration improves reaction kinetics according to the literature, but studying the effects was not covered in this work. We recommend to investigate the effect of KOH concentration in the Coval electrolyser.

Cell geometry, material properties and operating conditions are important factors for bubble management. Electrolyte and electrode properties can be changed in order to influence the nucleation behaviour. This option can be included in further research, as it has now been disregarded.

When tuning the operation conditions, the following guidelines of the literature are important. The electrolyte velocity should be sufficiently high: (i) to keep the ohmic voltage drop low, (ii) to prevent secondary reaction, (iii) to prevent nucleation, and (iv) to keep the bubble diameter low.

Increasing the electrode surface area can increase the reaction rate. In the literature techniques are mentioned to increase the specific electrode surface area. It is recommended to investigate the applicability of those techniques and what potential the techniques have to increase reaction rate.

This work brings Coval a step closer to commercialization of the technology to convert CO_2 electrochemically towards formic acid. Commercialization requires an economically viable and reliable technology. This study has provided a better understanding of the factors that influence the liquid distribution in the electrolyser. It has also contributed to a better insight into the behaviour of bubbles in the Coval electrolyser. This knowledge allowed to come up with new design ideas for the electrolyser cell. The new design ideas show promising flow distribution and bubble mitigation in an experimental setup. The next step is to implement those design ideas in the high pressure reactor.

Covalent technology allows for utilization of captured CO₂ and can play a key role in reducing the need for fossil sources. When fossil sources are not used any more, no new CO₂ will end up in the atmosphere. This will stabilize the carbon levels and reduce the effects of CO₂ on the climate.

Formic acid is a favourable energy carrier, because it contains both H₂ and CO, which can play an important role in energy storage. Electrochemically produced CO and formic acid have a positive business case for energy storage [4]. Reliable and sustainable power supply requires large-scale electricity storage, as most renewable energy sources are intermittent in their nature. This storage will become more important as the share of renewable energy is expected to grow [58]. Temporary surplus of renewable energy can be used for electrochemical reduction of CO₂ to formic acid, which can be used as an alternative for fossil sources.

Bibliography

- [1] U Desideri and F Asdrubali. Handbook of energy efficiency in buildings: a life cycle approach. Butterworth-Heinemann, 2018.
- [2] D Le Bideau, P Mandin, M Benbouzid, M Kim, M Sellier, F Ganci, and R Inguanta. Eulerian two-fluid model of alkaline water electrolysis for hydrogen production. *Energies*, 13:3394, 2020.
- [3] A Zarghami, NG Deen, and AW Vreman. CFD modeling of multiphase flow in an alkaline water electrolyzer. *Chemical Engineering Science*, 227:115926, 2020.
- [4] M Ramdin, A RT Morrison, M De Groen, R Van Haperen, R De Kler, E Irtem, A T Laitinen, L JP Van Den Broeke, T Breugelmans, JP M Trusler, et al. High-pressure electrochemical reduction of CO₂ to formic acid/formate: effect of pH on the downstream separation process and economics. *Industrial & Engineering Chemistry Research*, 58:22718–22740, 2019.
- [5] Z Tao, Z Wu, Y Wu, and H Wang. Activating copper for electrocatalytic CO₂ reduction to formate via molecular interactions. *ACS Catalysis*, 10:9271–9275, 2020.
- [6] Y Zhong, S Wang, M Li, J Ma, S Song, A Kumar, H Duan, Y Kuang, and X Sun. Rational design of copper-based electrocatalysts and electrochemical systems for CO₂ reduction: From active sites engineering to mass transfer dynamics. *Materials Today Physics*, page 100354, 2021.
- [7] Jos van der Maas. Exploring flow characteristics in a CO₂ electrolyser for producing formic acid - CFD modelling of the effect of flow rate and experimental validation, 2020.
- [8] M Fan, S Garbarino, A C Tavares, and D Guay. Progress in the electrochemical reduction of CO₂ on hierarchical dendritic metal electrodes. *Current Opinion in Electrochemistry*, pages 145–153, 2020.
- [9] T Burdyny and W A Smith. CO₂ reduction on gas-diffusion electrodes and why catalytic performance must be assessed at commercially-relevant conditions. *Energy & Environmental Science*, 12:1442–1453, 2019.
- [10] Q Lai, W Yuan, W Huang, and G Yuan. Sn/SnO_x electrode catalyst with mesoporous structure for efficient electroreduction of CO₂ to formate. *Applied Surface Science*, 508:145221, 2020.
- [11] Y Yang and F Li. Reactor design for electrochemical CO₂ conversion towards large scale applications. *Current Opinion in Green and Sustainable Chemistry*, page 100419, 2020.
- [12] A Senocrate and C Battaglia. Electrochemical CO₂ reduction at room temperature: Status and perspectives. *Journal of Energy Storage*, 36:102373, 2021.
- [13] J P Edwards, Y Xu, C M Gabardo, C Dinh, J Li, Z Qi, A Ozden, E H Sargent, and D Sinton. Efficient electrocatalytic conversion of carbon dioxide in a low-resistance pressurized alkaline electrolyzer. *Applied Energy*, 261:114305, 2020.
- [14] S Liang, N Altaf, L Huang, Y Gao, and Q Wang. Electrolytic cell design for electrochemical CO₂ reduction. *Journal of CO₂ Utilization*, 35:90–105, 2020.

- [15] W Zhang, Y Hu, L Ma, G Zhu, Y Wang, X Xue, R Chen, S Yang, and Z Jin. Progress and perspective of electrocatalytic CO₂ reduction for renewable carbonaceous fuels and chemicals. *Advanced Science*, 5:1700275, 2018.
- [16] D M Weekes, D A Salvatore, A Reyes, A Huang, and C P Berlinguette. Electrolytic CO₂ reduction in a flow cell. *Accounts of chemical research*, 51:910–918, 2018.
- [17] CERT Systems Inc. Our technology, 2021, <https://co2cert.com/about/cert-technology/> (Accessed: 2021-08-21).
- [18] Dioxide Materials. CO₂ conversion to formic acid, 2021, <https://dioxidematerials.com/technology/formic-acid/> (Accessed: 2021-08-21).
- [19] Opus 12. Technology, 2020, <https://www.opus-12.com/technology> (Accessed: 2021-08-21).
- [20] Siemens AG. A climate killer is turned into feedstock: Using CO₂ and hydrogen for sustainable chemicals, 2020, <https://www.siemens-energy.com/global/en/news/magazine/2020/rheticus-worlds-first-automated-co2-electrolyzer.html> (Accessed: 2021-08-21).
- [21] D Pletcher, Z Tian, and D Williams. *Developments in Electrochemistry*. Wiley Online Library, 2014.
- [22] R Cervantes-Alcala and M Miranda-Hernandez. Flow distribution and mass transport analysis in cell geometries for redox flow batteries through computational fluid dynamics. *Journal of applied electrochemistry*, 48:1243–1254, 2018.
- [23] Q Zheng, F Xing, X Li, G Ning, and H Zhang. Flow field design and optimization based on the mass transport polarization regulation in a flow-through type vanadium flow battery. *Journal of Power Sources*, 324:402–411, 2016.
- [24] L Vázquez, A Alvarez-Gallegos, FZ Sierra, C P De León, and FC Walsh. CFD evaluation of internal manifold effects on mass transport distribution in a laboratory filter-press flow cell. *Journal of Applied Electrochemistry*, 43:453–465, 2013.
- [25] FJ Recio, P Herrasti, L Vazquez, C P de León, and FC Walsh. Mass transfer to a nanostructured nickel electrodeposit of high surface area in a rectangular flow channel. *Electrochimica Acta*, 90:507–513, 2013.
- [26] B Zayat, D Mitra, and SR Narayanan. Inexpensive and efficient alkaline water electrolyzer with robust steel-based electrodes. *Journal of The Electrochemical Society*, 167:114513, 2020.
- [27] İ Dinçer and C Zamfirescu. *Sustainable hydrogen production*. Elsevier, 2016.
- [28] Á Frías-Ferrer, J González-García, V Sáez, C P de León, and F C Walsh. The effects of manifold flow on mass transport in electrochemical filter-press reactors. *AIChE Journal*, 54:811–823, 2008.
- [29] S K Karode and A Kumar. Flow visualization through spacer filled channels by computational fluid dynamics i.: Pressure drop and shear rate calculations for flat sheet geometry. *Journal of Membrane science*, 193:69–84, 2001.
- [30] E Askari, P Proulx, and A Passalacqua. Modelling of bubbly flow using CFD-PBM solver in OpenFOAM: study of local population balance models and extended quadrature method of moments applications. *ChemEngineering*, 2:8, 2018.

- [31] P Boissonneau and P Byrne. An experimental investigation of bubble-induced free convection in a small electrochemical cell. *Journal of Applied Electrochemistry*, 30:767–775, 2000.
- [32] Y Fukunaka, K Suzuki, A Ueda, and Y Kondo. Mass-transfer rate on a plane vertical cathode with hydrogen gas evolution. *Journal of The Electrochemical Society*, 136:1002, 1989.
- [33] J Lee, D K Sohn, and H S Ko. Study on bubble visualization of gas-evolving electrolysis in forced convective electrolyte. *Experiments in Fluids*, 60:1–11, 2019.
- [34] P K. Kundu, I M. Cohen, and D R. Dowling. *Fluid Mechanics (Sixth Edition)*. Academic Press, 2016.
- [35] G Espinasse, M Peyrard, F Nicolas, and J Caire. Effect of hydrodynamics on faradaic current efficiency in a fluorine electrolyser. *Journal of applied electrochemistry*, 37:77–85, 2007.
- [36] H Vogt. The rate of gas evolution of electrodes—I. An estimate of the efficiency of gas evolution from the supersaturation of electrolyte adjacent to a gas-evolving electrode. *Electrochimica acta*, 29:167–173, 1984.
- [37] H Vogt. Studies on gas-evolving electrodes: The concentration of dissolved gas in electrolyte bulk. *Electrochimica acta*, 30:265–270, 1985.
- [38] D Zhang and K Zeng. Evaluating the behavior of electrolytic gas bubbles and their effect on the cell voltage in alkaline water electrolysis. *Industrial & Engineering Chemistry Research*, 51:13825–13832, 2012.
- [39] LJJ Janssen, CWMP Sillen, E Barendrecht, and SJD Van Stralen. Bubble behaviour during oxygen and hydrogen evolution at transparent electrodes in koh solution. *Electrochimica acta*, 29:633–642, 1984.
- [40] H Vogt. Frictional pressure drop of pure and contaminated bubble-electrolyte dispersions in electrochemical reactors. *Journal of applied electrochemistry*, 13:705–707, 1983.
- [41] A Rahbari, J Brenkman, R Hens, M Ramdin, L.J.P. van den Broeke, R Schoon, R Henkes, O.A. Moulto, and T.J.H. Vlugt. Solubility of water in hydrogen at high pressures: a molecular simulation study. *Journal of Chemical & Engineering Data*, 64:4103–4115, 2019.
- [42] P T Moseley and J Garche. *Electrochemical energy storage for renewable sources and grid balancing*. Newnes, 2014.
- [43] H Vogt. The problem of the departure diameter of bubbles at gas-evolving electrodes. *Electrochimica acta*, 34:1429–1432, 1989.
- [44] H Vogt. A hydrodynamic model for the ohmic interelectrode resistance of cells with vertical gas evolving electrodes. *Electrochimica Acta*, 26:1311–1317, 1981.
- [45] H Vogt. The incremental ohmic resistance caused by bubbles adhering to an electrode. *Journal of Applied Electrochemistry*, 13:87–88, 1983.
- [46] R Phillips and C W Dunnill. Zero gap alkaline electrolysis cell design for renewable energy storage as hydrogen gas. *RSC advances*, 6:100643–100651, 2016.
- [47] J Kim, J Lee, C Yoo, K Lee, and W Lee. Low-cost and energy-efficient asymmetric nickel electrode for alkaline water electrolysis. *International journal of hydrogen energy*, 40:10720–10725, 2015.

-
- [48] D Pletcher and X Li. Prospects for alkaline zero gap water electrolyzers for hydrogen production. *International Journal of Hydrogen Energy*, 36:15089–15104, 2011.
- [49] N Nagai, M Takeuchi, T Kimura, and T Oka. Existence of optimum space between electrodes on hydrogen production by water electrolysis. *International journal of hydrogen energy*, 28:35–41, 2003.
- [50] J Houser, A Pezeshki, J T Clement, D Aaron, and M M Mench. Architecture for improved mass transport and system performance in redox flow batteries. *Journal of Power Sources*, 351:96–105, 2017.
- [51] J St-Pierre and A A Wragg. Behaviour of electrogenerated hydrogen and oxygen bubbles in narrow gap cells—part i. experimental. *Electrochimica acta*, 38:1381–1390, 1993.
- [52] P Hadikhani, S M H Hashemi, and D Psaltis. The impact of surfactants on the inertial separation of bubbles in microfluidic electrolyzers. *Journal of The Electrochemical Society*, 167:134504, 2020.
- [53] M D Mat, K Aldas, and O J Ilegbusi. A two-phase flow model for hydrogen evolution in an electrochemical cell. *International Journal of Hydrogen Energy*, 29:1015–1023, 2004.
- [54] K Ito, Y Maeda, T Sakaguchi, S Tsukamoto, A Inada, Y Tsuchiya, and H Nakajima. Analysis and visualization of water flow impact on hydrogen production efficiency in solid polymer water electrolyzer under high-pressure condition. *International Journal of Hydrogen Energy*, 40:5995–6003, 2015.
- [55] F M White. *Fluid Mechanics, in SI Units*. McGraw-Hill, New York, 2016.
- [56] ANSYS Inc. *ANSYS Fluent User’s Guide*, 2018, <https://www.ansys.com/products/fluids/ansys-fluent> (Accessed: 2021-08-21).
- [57] Granta Design Limited. *Granta edupack 2020 version: 20.1.1*. <https://software.tudelft.nl/457/>, 2020.
- [58] WJ van Egmond, M Saakes, I Noor, S Porada, CJN Buisman, and HVM Hamelers. Performance of an environmentally benign acid base flow battery at high energy density. *International Journal of Energy Research*, 42:1524–1535, 2018.

A. 2D drawings

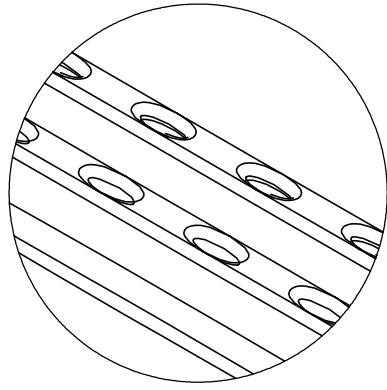
The next pages show drawings of the prototypes: (i) the spacer with manifold, and (ii) the electrode with channels. The spacer with the manifold in the calm zone showed the most promising results in the experimental setup for fluid distribution. This design has a baffle followed by two full width bars with oval holes in the bottom calm zone. A single bar with oval holes is located in the top calm zone.

The electrode with channels is an assembly of milled electrodes with printed inserts. The ribs between the channels reduce locally the interelectrode distance. The simulation showed auspicious results for the fluid distribution over the cell width when channels were applied. The printed inserts can be exchanged to adjust the zone before and after the channels. For example, inserts with a manifold can be placed.

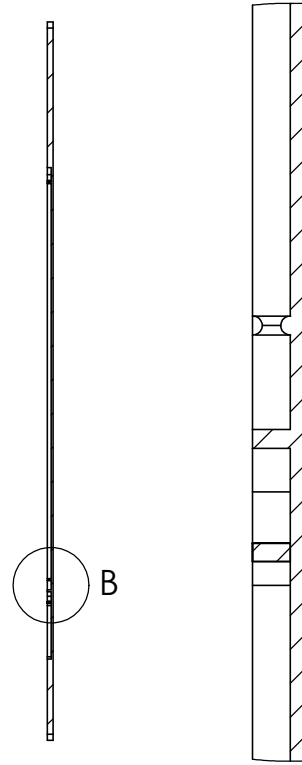
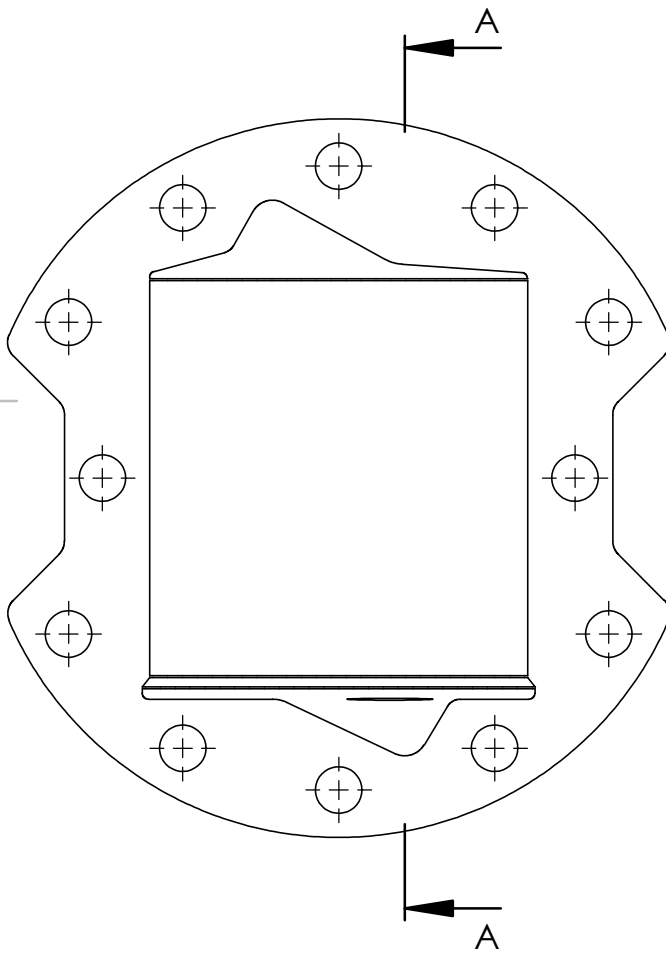
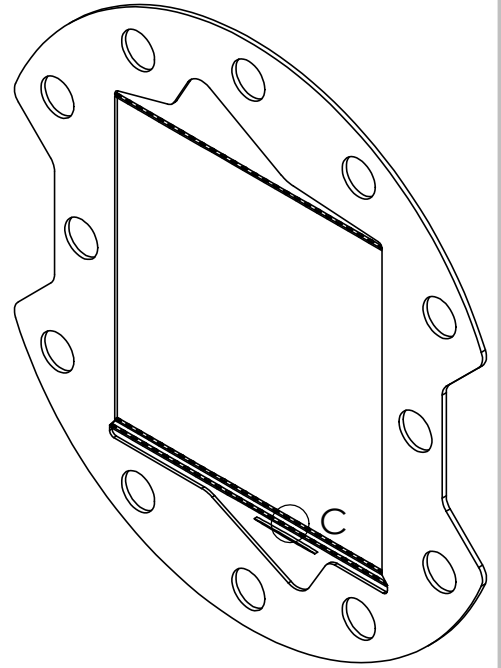
4 3 2 1

F
E
D
C
B

F
E
D
C
B



DETAIL C
SCALE 5 : 1



SECTION A-A DETAIL B
SCALE 5 : 1

UNLESS OTHERWISE SPECIFIED:
DIMENSIONS ARE IN MILLIMETERS
SURFACE FINISH:
TOLERANCES:
LINEAR:
ANGULAR:

FINISH:

DEBURR AND
BREAK SHARP
EDGES

DO NOT SCALE DRAWING

REVISION

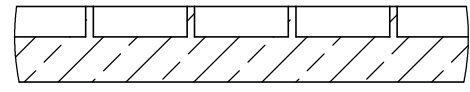
	NAME	SIGNATURE	DATE
DRAWN			
CHK'D			
APPV'D			
MFG			
Q.A			
MATERIAL:			
Material <not specified>			
WEIGHT:			

TITLE:	<h1>CZ1spacerB</h1>
DWG NO.	
SCALE:1:2	SHEET 1 OF 1

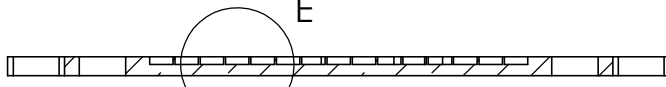
A4

A

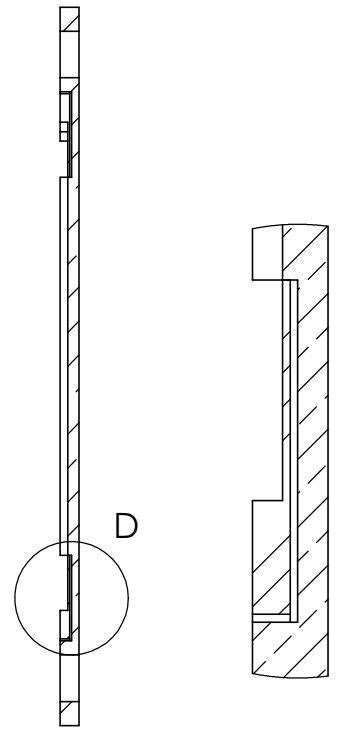
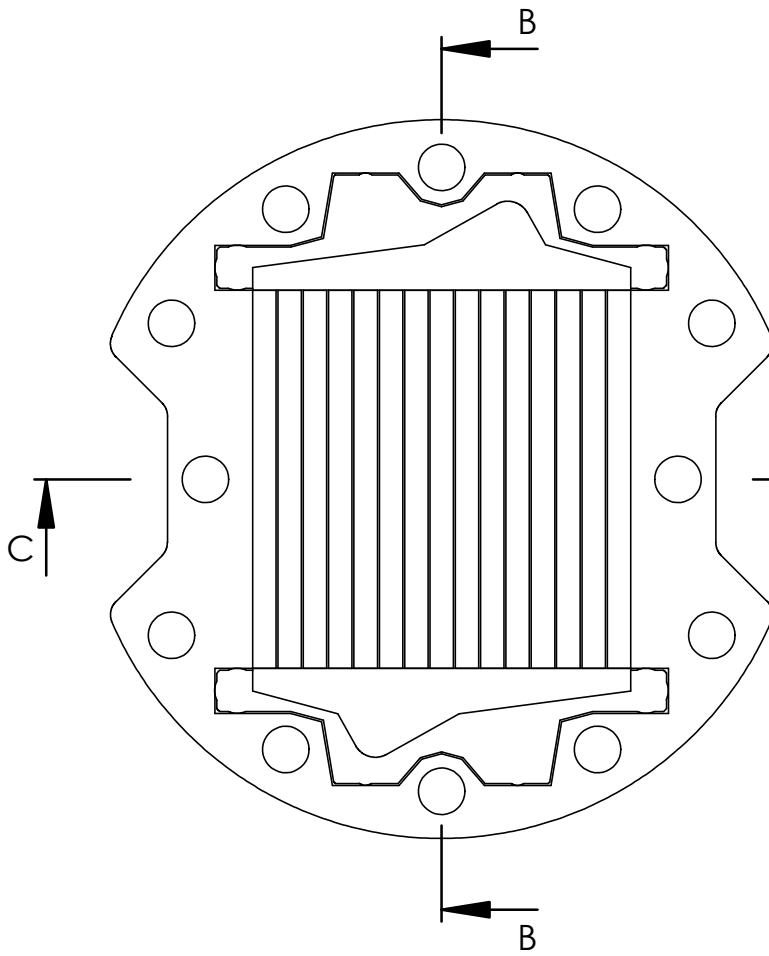
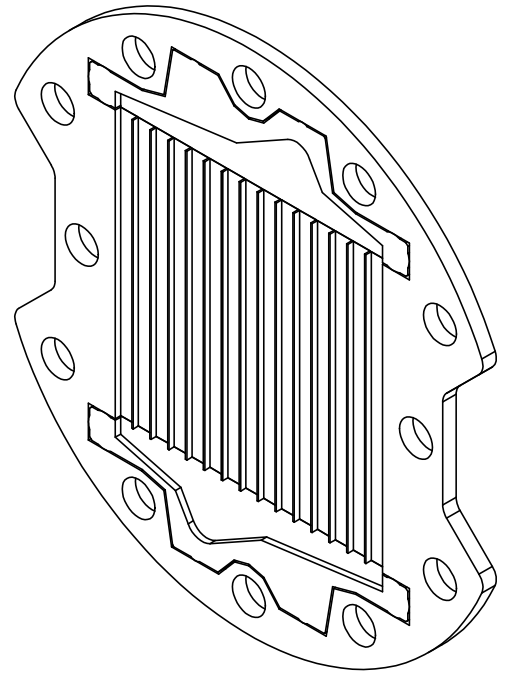
4 3 2 1



DETAIL E
SCALE 2 : 1



SECTION C-C



SECTION B-B
DETAIL D
SCALE 2 : 1

UNLESS OTHERWISE SPECIFIED:
DIMENSIONS ARE IN MILLIMETERS
SURFACE FINISH:
TOLERANCES:
LINEAR:
ANGULAR:

FINISH:

DEBURR AND
BREAK SHARP
EDGES

DO NOT SCALE DRAWING

REVISION

	NAME	SIGNATURE	DATE	
DRAWN				
CHK'D				
APPV'D				
MFG				
Q.A				
				MATERIAL:
				WEIGHT:

TITLE:	
DWG NO.	
ch+ins	
SCALE: 1:2	SHEET 1 OF 1

A4